Simulations of sphere-forming diblock copolymer melts

Anshul Chawla, Frank S. Bates, Kevin D. Dorfman,* and David C. Morse[†]

Department of Chemical Engineering and Materials Science,

University of Minnesota – Twin Cities,

421 Washington Ave. SE, Minneapolis, MN 55455, USA

Abstract

Molecular dynamics simulations are used to study melts of asymmetric sphere-forming diblock copolymers with two significantly different values of the invariant degree of polymerization, $\overline{N}=3820$ and 960. In both systems, changes in parameters that correspond to decreasing temperature lead to the appearance of micelles at a critical micelle temperature (CMT) and crystallization at a lower order-disorder transition temperature (ODT). The CMT is identifiable in simulations by the appearance of large clusters with a strongly segregated core region, but has no equally clear signature in scattering experiments on systems of modest \overline{N} . The value of the product χN at the CMT (where χ is the Flory-Huggins parameter and N is degree of polymerization) is close to that predicted by SCFT for the ODT, while the value at the actual ODT is larger and increases with decreasing \overline{N} . Micelles exhibit significant and comparable dispersity in aggregation number in the crystalline and liquid phases near the ODT. Both the liquid and crystal phases exhibit transient dimers consisting of pairs of neighboring spherical micelles with cores connected by a bridge of core-block material.

^{*} dorfman@umn.edu

[†] morse012@umn.edu

I. INTRODUCTION

Melts of highly asymmetric AB diblock copolymers tend to self-assemble into spherical micelles with a core containing the minority block. A variety of experiments and simulations [1–8] suggest the existence of three temperature regimes in systems with a positive heat of mixing (the usual case): The high temperature regime produces a molecularly disordered state with relatively small composition fluctuations. With decreasing temperature, micelles appear over a relatively narrow range of temperatures near a critical micelle temperature (CMT), forming a liquid of micelles over an intermediate temperature range. Upon further decreasing temperature, this liquid crystallizes at an order-disorder transition temperature (ODT), creating an ordered phase. The most commonly observed crystalline arrangement of micelles is a body-centered cubic (BCC) lattice, but a variety of more complicated Frank-Kasper and quasi-crystalline arrangements have been observed [9–19].

Three different types of experiments have provided evidence for the existence of a liquid of micelles over a range of temperatures above the ODT. First, several early transmission electron microscopy (TEM) images showed a dense, disordered arrangement of spherical micelles at temperatures above the ODT [6, 7]. Second, results of small angle X-ray and neutron scattering (SAXS and SANS) experiments in the liquid phase near the ODT show the presence of a secondary peak or shoulder in plots of scattering intensity I(q) vs. scattering wavenumber q, consistent with the picture of a disordered micellar phase [1–5]. An early analysis by Kinning and Thomas [1] showed that the existence and approximate position of this secondary feature could be explained by a model of the melt as a strong correlated liquid of spherical micelles, using the Percus-Yevick theory of hard spheres [20] to model a structure function factor that describes correlations in micelle center-of-mass positions. This analysis was repeated and refined in several subsequent scattering studies [2–5]. Finally, measurements of linear viscoelastic properties have also shown the existence of an elastic-like response at high frequencies that is believed to be the result of stress created by straining a disordered micro-phase separated state [21].

Establishing the theoretical basis for the disordered micelle regime has been a longstanding challenge. To establish notation, consider an incompressible melt of AB diblock polymers with degree of polymerization N, volume fraction f for the minority block, Flory-Huggins parameter χ , statistical segment lengths b_A and b_B for A and B monomers, respectively,

and a total monomer concentration c=1/v, where v is a monomer reference volume. Let g denote the free energy per polymer divided by kT, where k is Boltzmann's constant and T is absolute temperature. Self-consistent field theory (SCFT), the most widely used theory for describing block polymer phase behavior, yields a prediction for g in a given phase that depends only on the dimensionless parameters χN , f, and b_A/b_B , which we refer to as the SCFT state parameters. We focus hereafter on conformationally symmetric systems with $b_A=b_B=b$, for which the remaining state parameters are χN and f. SCFT predictions for structural lengths such as the micelle core radius and equilibrium unit cell dimensions in a crystalline phase of such a system are given by R times a dimensionless function of the same state parameters, where $R=b\sqrt{N}$ is the end-to-end distance of the polymer. SCFT predicts the simultaneous appearance and crystallization of micelles at a first-order transition from a micelle-free disordered phase to a crystal of micelles. This predicted order-disorder transition occurs at a critical value of χN , denoted here by $(\chi N)_{\rm odt}^{\rm scf}$, that depends only on f. The systems simulated here all have f=0.125 for which $(\chi N)_{\rm odt}^{\rm scf}=36.6$ [22].

The magnitude and nature of deviations from SCFT predictions for block copolymer melts are controlled by the invariant degree of polymerization $\overline{N} = N(cb^3)^2$. The parameter $\overline{N}^{1/2}$ is proportional to the ratio R^3/Nv of the volume R^3 pervaded by a random walk polymer to the occupied volume per chain Nv. Theoretical analyses [23–25] and simulations of simple models [26–32] both suggest that SCFT becomes exact in the limit $\overline{N} \to \infty$, and that deviations from SCFT exhibit a universal dependence on \overline{N} , independent of many details of a particular simulation model or experimental system. Specifically, simulations of symmetric and modestly asymmetric diblock copolymers have provided strong evidence for the hypothesis that g is a nearly universal function of \overline{N} and the SCFT state parameters [29, 30, 32]. However, SCFT is based on a qualitatively incorrect picture of the disordered phase near the ODT because it assumes random mixing at a monomer level within the disordered phase. In systems with experimentally relevant values of \overline{N} , the disordered phase of a diblock copolymer melt near the ODT is instead found to contain disordered but rather strongly segregated A and B domains [29, 30, 33]. Highly asymmetric copolymers with f < 0.2 such as those simulated here, form disordered arrangements of spherical micelles [1-7]. The appearance of local segregation without crystalline order stabilizes the disordered phase, and pushes the value of χN at the actual order-disorder transition $(\chi N)_{\rm odt}$ to values significantly greater than $(\chi N)_{\text{odt}}^{\text{scf}}$

There are two key prior theoretical studies of the disordered micelle regime that are relevant to the present work. In the first, Dormidontova and Lodge presented a relatively simple and qualitatively correct theory of thermodynamics in sphere-forming diblock copolymers that predicts the existence of a micellar liquid regime at intermediate temperatures [34]. This theory extended earlier work by Semenov [35, 36] on a strong-stretching theory for asymmetric copolymers, which provided analytic expressions for both the free energy of an isolated micelle and for an effective interaction between pairs of micelles. Dormidontova and Lodge [34] combined this with a simple treatment of the effects of micelle and unimer translational entropy, and allowed for the possible formation of a disordered micellar fluid. The resulting theory yields predictions for both an apparent CMT and the ODT. In the second relevant study, Wang et al. presented an analysis of the appearance of micelles within the disordered phase that is based upon a numerical SCFT calculation of the free energy of formation of an isolated micelle within an otherwise disordered melt [33]. This formation free energy, denoted here by W_m , becomes negative at values of χN greater than a critical value, denoted here by $(\chi N)_{\rm m}^{\rm scf}$, thus favoring the proliferation of micelles for $\chi N > (\chi N)_{\rm m}^{\rm scf}$. The value of $(\chi N)_{\rm m}^{\rm scf}$ was found to be very similar but slightly greater than the value $(\chi N)_{\rm odt}^{\rm scf}$ at which SCFT predicts formation of a crystal to become favorable. The slight difference reflects the fact that the crystal phase is stabilized by the existence of weak attractions between neighboring micelles in a crystal. For example, for the case f = 0.1 that they studied in greatest detail, Wang et al. found $(\chi N)_{\rm m}^{\rm scf}=48.14$, while we obtain $(\chi N)_{\rm odt}^{\rm scf}=47.95$ for a BCC crystal candidate phase. The difference $(\chi N)_{\rm m}^{\rm scf} - (\chi N)_{\rm odt}^{\rm scf}$ is, however, much smaller than other differences of interest here, such as the difference $(\chi N)_{\text{odt}} - (\chi N)_{\text{odt}}^{\text{scf}}$, and so is negligible for our current purposes.

In the present contribution, we report data for coarse-grained bead-spring diblock copolymer melt simulations performed for two models with significantly different values of \overline{N} . We recently provided a preliminary report [8] for a system with $\overline{N}=3820$, focusing on the development of methods to identify the CMT. Here, we present a more thorough analysis of those data [8] and new data for a system with $\overline{N}=960$, with the latter system bringing to the fore the impact of fluctuation effects that should be prominent for experimentally-relevant degrees of polymerization. Where appropriate, we reproduce some results reported in Ref. [8] alongside new data for $\overline{N}=960$ so that the impact of lowering \overline{N} is readily discernible. The analysis presented here involves a detailed structural characterization, comparisons to

SCFT predictions, and analyses of both ordered and disordered phases. In addition to the additional data at low \bar{N} and the accompanying discussion that did not appear in Ref. [8], this contribution provides an interpretation of the structure factor in the context of Percus-Yevick theory [20], calculation of the number of free chains, comparison of the most probable aggregation number to an estimate from SCFT, computation of the latent heat at the ODT [37], and a thorough analysis of dimer formation in both the ordered and disordered state, including an analysis of their dynamics [37].

II. SIMULATION DETAILS

In this work we have used constant pressure, constant temperature molecular dynamics (MD) simulations of coarse-grained bead-spring models of asymmetric AB diblock copolymers. Each chain contains N beads, of which $N_B = fN$ are of monomer type B (the minority species), and the remainder of type A. For all systems studied in this work, N = 64 and $N_B = 8$, giving f = 1/8.

We use a potential energy with a harmonic bond potential and a soft nonbonded pair interaction similar to that introduced in dissipative particle dynamics simulations, employing choices of parameters used in several previous simulation studies by our group [29–32]. A repulsive non-bonded potential acts between all bead pairs that are separated by a distance r less than a cutoff distance σ , with a potential of the form $\epsilon_{ij}[1-(r/\sigma)]^2/2$ between beads of types i and j for $r < \sigma$, with $\epsilon_{AA} = \epsilon_{BB}$. We define a parameter $\alpha \equiv (\epsilon_{AB} - \epsilon_{AA})/k_BT$ that is adjusted to control the driving force for microphase separation. Adjacent beads within each chain interact via a harmonic bond potential of the form $\kappa r^2/2$, where κ is a spring constant. Additional details on the simulation method are provided in the Supplementary Material [37].

We simulate two systems, each of which is defined by a fixed set of choices for all model parameters except α , and simulate each system over a range of values of α . The two systems studied here correspond to models S1-64 and S2-64 as defined in Ref. [30]. These models have previously [29, 30] been shown to yield invariant degrees of polymerization $\overline{N} = 960$ (S1-64) and $\overline{N} = 3820$ (S2-64). For clarity in what follows, we will refer to the different simulation systems by their invariant degrees of polymerization since this is the physically relevant descriptor. Previous work [29, 30] further established a relationship between α and

TABLE I. Model parameters and properties for models S1 and S2, in units with $k_{\rm B}T=\sigma=1$. The self-interaction parameter ϵ_{AA} , spring stiffness κ , and pressure P have fixed values for each model. The monomer concentration c and statistical segment length b are extrapolated values for infinite homopolymers ($\alpha=0$ and $N\to\infty$). The quantities z, a and d are coefficients that appear in Eq. (1) for $\chi(\alpha)$.

Model

$$\epsilon_{AA}$$
 κ
 c
 P
 b
 z
 a
 d

 S1
 25.0
 3.406
 3.0
 20.249
 1.088
 0.237
 0.138
 0.438

 S2
 25.0
 1.135
 1.5
 4.111
 1.727
 0.0916
 -0.00087
 0.00420

the Flory-Huggins interaction parameter χ for each of these models, which was approximated by the function

$$\chi(\alpha) = \frac{z\alpha + a\alpha^2}{1 + d\alpha} \quad . \tag{1}$$

Table I lists values for the fixed input parameters for the two models studied in this work, along with values of the coefficients z, a and d and other properties that were obtained in previous work [29, 30] by analyzing simulations of these models; the reader is referred to Ref. [30] for a detailed explanation of the model parameters.

We have also performed simulations to identify conditions under which an initially disordered melt will spontaneously crystallize or an initially ordered crystal will spontaneously melt in systems that are designed so that the periodic simulation unit cell is, as nearly as possible, commensurate with the preferred crystallographic unit cell. The latter results and a discussion on the latent heat of the transition are provided as Supplementary Material [37]. The number of polymer molecules, denoted by M, was chosen in most simulations so as to approximately accommodate a $3 \times 3 \times 3$ array of BCC unit cells if the system were to crystallize [37].

Much of our analysis relies on the identification of physical clusters of molecules that are candidates for identification as micelles. Two molecules are taken to belong to the same cluster if their minority blocks are in close contact, i.e., if the distance between any intermolecular pair of minority block beads from these molecules is less than 0.8σ . This value was selected based on prior simulations of micelles using these models [38], where aggregation numbers using this cutoff were consistent with those obtained by counting the number of

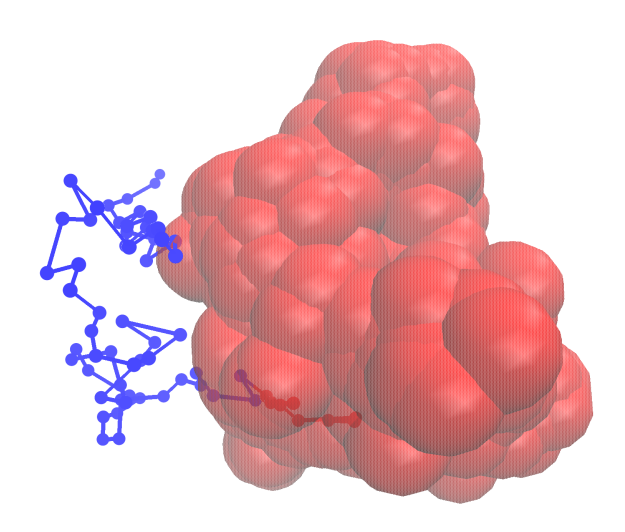


FIG. 1. Visualization of the core of a micellar cluster composed of 83 chains. Minority block beads belonging to all molecules in the cluster are shown as as overlapping translucent red spheres. The conformation of one representative molecule is shown as sequence of points representing beads connected by line segments, with blue points for majority/corona block beads and red points for minority/core block beads.

chains in a micelle. Using this criterion, we may assign every molecule in the system to a unique cluster. Fig. 1 shows a visualization of a micellar cluster identified by this method, in a format that shows the micelle core and the conformation of one molecule.

III. STRUCTURE FACTOR

The structure factor S(q) is defined here as

$$S(q) = \left\langle \frac{1}{V} |\tilde{\psi}(\mathbf{q})|^2 \right\rangle \quad , \tag{2}$$

where $\tilde{\psi}(\mathbf{q}) = \int d\mathbf{r} \ \psi(\mathbf{r}) e^{i\mathbf{q}\cdot\mathbf{r}}$ is a Fourier amplitude of the composition field $\psi(\mathbf{r}) = [c_A(\mathbf{r}) - c_B(\mathbf{r})]/2$, $c_i(\mathbf{r})$ is the concentration of i monomers, V is total system volume, and $q = |\mathbf{q}|$. Fig. 2 compares S(q) data for different values of χN for both $\overline{N} = 960$ and the previous data [8] for $\overline{N} = 3820$. The most obvious feature in this figure is the existence of a maximum in S(q) at a wavenumber denoted by q^* .

To identify any secondary features, we fit the data in Fig. 2 to a functional form $S(q) = KS_{RPA}(q)$, where $S_{RPA}(q)$, the solid lines in Fig. 2, are the prediction of the random-phase

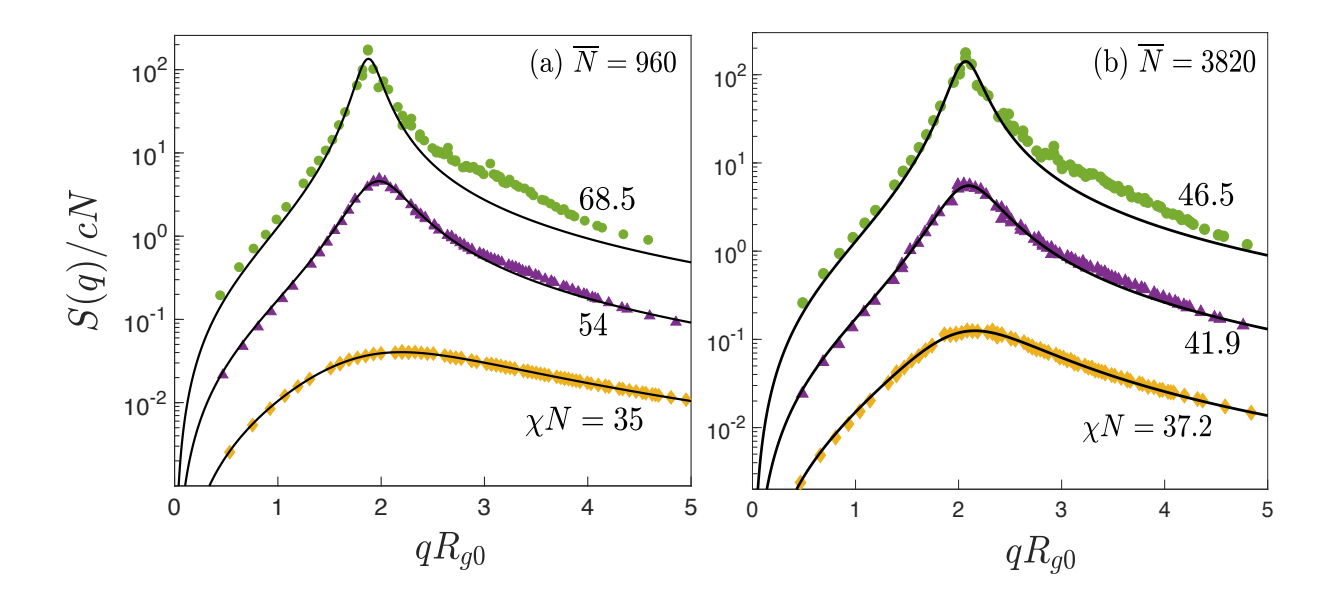


FIG. 2. Structure factor S(q) vs. non-dimensionalized wavenumber qR_{g0} , for (a) $\overline{N} = 960$ and (b) $\overline{N} = 3820$ at several values of χN . $R_{g0} = b\sqrt{N/6}$ is the unperturbed polymer radius of gyration. Solid lines are fits of behavior near the peak to the functional form predicted by the random-phase approximation (RPA). Panel (b) reproduced with permission from Ref. [8].

approximation (RPA) [39]. In this fit, the prefactor K and the parameters R_g and χ that are required as inputs to the RPA prediction have all been treated as adjustable parameters that are chosen to fit the data in the vicinity of the peak. The RPA functional fits the data for both models at the lowest value of χN , which in both cases is near $(\chi N)_{\text{odt}}^{\text{sef}} = 36.6$, but the RPA does not fit the results for higher values of χN for neither value of \overline{N} . Comparison of the data to this fit helps emphasize the appearance at higher values of χN of a weak shoulder centered around $qR_{g0} \sim 3$ -4, where $R_{g0} = b\sqrt{N/6}$ is the unperturbed radius of gyration, which becomes more prominent with increasing χN . The existence of this secondary feature in S(q) was first noted in experimental scattering data by Kinning and Thomas [1], who attributed it to the presence of strong correlations in the positions of micelles within a dense micellar liquid. This secondary shoulder develops at significantly lower values of χN in the system with larger value of \overline{N} ; note that the strength of the shoulder in the system with $\overline{N} = 3820$ and $\chi N = 46.5$ (Fig. 2b) is greater than that seen in the system $\overline{N} = 960$ (Fig. 2a) at a higher value of $\chi N = 54$, and comparable to that observed for $\overline{N} = 960$ at the much higher value of $\chi N = 68.5$.

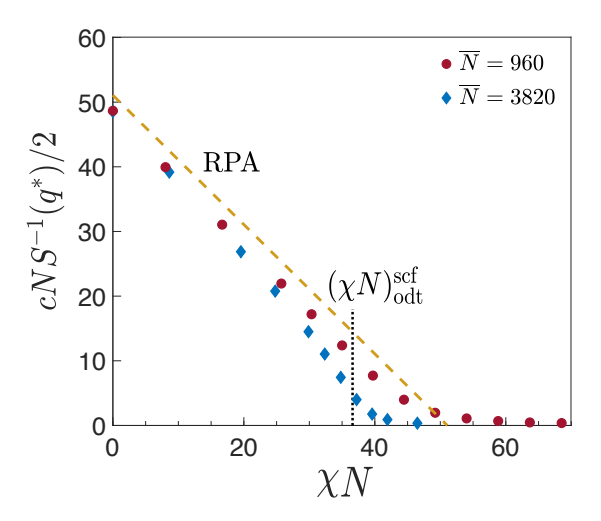


FIG. 3. Non-dimensionalized inverse peak intensity $cNS^{-1}(q^*)/2$ vs. χN for $\overline{N}=960$ (solid red circles) and $\overline{N}=3820$ (solid blue diamonds). The diagonal dashed line is the RPA prediction. The vertical dotted line marks location of $(\chi N)_{\rm odt}^{\rm scf}$. Error bars are smaller than the data points and provided in the Supplementary Material [37].

To discern the deviations between the RPA model and the simulation data across the full range of χN , Fig. 3 shows how the normalized inverse peak intensity $cNS^{-1}(q^*)/2$ within the disordered phase changes with χN for both invariant degrees of polymerization. The results for $\overline{N} = 3820$ have been reported previously [8]. A strongly first-order ODT of the type predicted by SCFT would be accompanied by a dramatic increase in $S(q^*)$, and a corresponding decrease in $S^{-1}(q^*)$, due to the appearance of Bragg peaks in S(q). Appearance and proliferation of disordered micelles within a sufficiently narrow range of values of χN near $(\chi N)_{\mathrm{odt}}^{\mathrm{scf}}$ also would be expected to produce a sudden increase in $S(q^*)$, or, equivalently, a sudden decrease in $S^{-1}(q^*)$, with increasing χN , due to the appearance of additional scattering from micelles. A hint of this type of behavior is visible in Fig. 3 for $\overline{N} = 3820$, which exhibits an inflection at a value of χN near $(\chi N)_{\rm odt}^{\rm scf}$ at which the magnitude of the slope $dS^{-1}(q^*)/d(\chi N)$ appears to show a weak maximum. There is, however, no sign of such an inflection in corresponding results for $\overline{N} = 960$. Rather, $S^{-1}(q^*)$ vs. χN exhibits a uniformly positive curvature and flattening out near an apparent spinodal value analogous to that seen in corresponding plots of results for more symmetric copolymers [26, 28, 40]. This difference in the behavior of the peak intensity in systems with different values of Nsuggests that micelles proliferate over a smaller range of values of χN in systems with larger

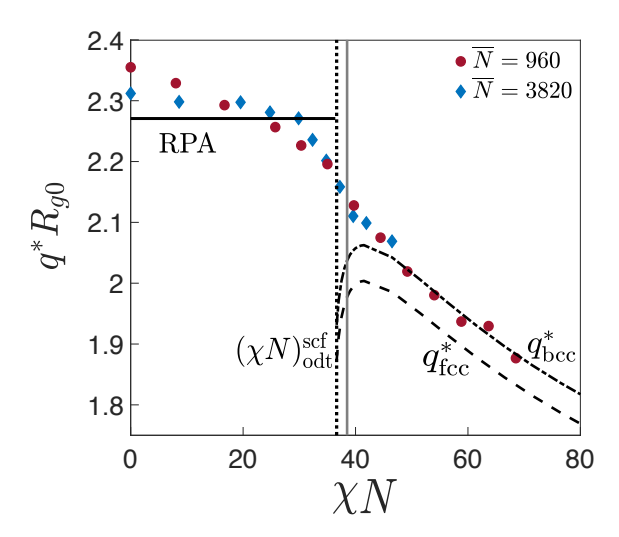


FIG. 4. Normalized peak wavenumber q^*R_{g0} vs. χN for $\overline{N}=960$ (solid circles) and $\overline{N}=3820$ (solid blue diamonds), where $R_{g0}=b\sqrt{N/6}$. The dotted vertical line and the solid vertical gray line marks the disordered-FCC phase transition at $(\chi N)_{\rm odt}^{\rm scf}=36.6$ and the order-order transition from FCC to BCC at $\chi N=38.5$, respectively. The solid horizontal black line shows the RPA prediction for q^*R_{g0} in the disordered phase, which is shown only for $\chi N<(\chi N)_{\rm odt}^{\rm scf}$. The dotdashed and dashed curves plotted for $\chi N>(\chi N)_{\rm odt}^{\rm scf}$ show SCFT predictions for the value of q^*R_{g0} corresponding to the primary Bragg peaks in the BCC and FCC phases, respectively.

values of \overline{N} .

The location of the structure factor peak at q^* provides further information on the intermicellar distance. Figure 4 thus compares simulation results for both invariant degrees of polymerization to (i) RPA predictions for q^* for $\chi N < (\chi N)_{\text{odt}}^{\text{scf}}$ and (ii) SCFT predictions for the wavenumber of the primary family of Bragg peaks for $\chi N > (\chi N)_{\text{odt}}^{\text{scf}}$, where q^* is made dimensionless with R_{g0} . The results for $\overline{N} = 3820$ have been reported previously [8]. Data for both values of \overline{N} exhibit a monotonic decrease of q^* with increasing χN . Values of q^* at $\chi N = 0$ are slightly greater than those predicted by the RPA for both models, with closer agreement between the RPA prediction for $\chi N < (\chi N)_{\text{odt}}^{\text{scf}}$ and the larger \overline{N} . For $\chi N > (\chi N)_{\text{odt}}^{\text{scf}}$, simulation results for q^* in the disordered phase seem to approach the SCFT predictions for the BCC phase that SCFT predicts to be stable over most of this range. This behavior of q^* is broadly analogous to that seen in previous simulations of the disordered phase of less asymmetric copolymers [28, 31].

The structure factor S(q) measured here is analogous to the scattering intensity I(q) measured in small-angle x-ray and neutron scattering studies. In an analysis that was introduced by Kinning and Thomas [1] and refined in subsequent work [2, 3, 5, 7], I(q) in the disordered phase of asymmetric copolymers was modeled as scattering from a liquid of spherical micelles. In those analyses, experimental data for I(q) are compared to a model in which S(q) is expressed as a product of a form factor for a spherical micelle core times a structure factor for the centers of the micelle cores, denoted here by Z(q). The Percus-Yevick (PY) theory for hard spheres [20] is used to model the micelle structure factor Z(q), while treating the sphere radius and effective volume fraction as adjustable parameters. The resulting model was shown [1–5] to account naturally for the appearance of a primary peak and secondary shoulder in S(q) with approximately the observed ratio of characteristic wavenumbers, in a model in which both features are assumed to be consequences of intermicellar correlations in a dense fluid.

Using our simulation data, we can directly measure the relevant micelle structure function Z(q), and thereby test the assumptions underlying this analysis. Our calculation of Z(q) is based on an analysis of "micellar" clusters, defined as clusters for which the aggregation number lies within a specific range of values using the algorithm described in Section II. Let x_n denote the fraction of chains that belong to clusters of aggregation number n. In systems that contain well defined micelles, the distribution x_n exhibits a local minimum and a local maximum, as discussed in detail in Section IV. To compute Z(q), micellar clusters are taken to be those for which the aggregation number n lies between the value at which x_n exhibits a local minimum and 1.6 times the value at the local maximum. For each such micellar cluster, we define a central position defined as the center-of-mass of the minority block beads of molecules that belong to the cluster (i.e., the center of mass of the core). The micelle structure function Z(q) is then defined by the sum

$$Z(q) = \sum_{j,k} \left\langle \frac{1}{V} e^{i\mathbf{q} \cdot (\mathbf{R}_j - \mathbf{R}_k)} \right\rangle , \qquad (3)$$

where \mathbf{R}_j represents the central position of micellar cluster number j. The sums over j and k are taken over all micellar clusters.

Figure 5 provides simulation results for Z(q) for two values of χN for each of the two values of \overline{N} . For each value of \overline{N} , the higher value of χN shown corresponds to a state in which S(q) exhibits both a primary peak and a clear secondary shoulder. The corresponding

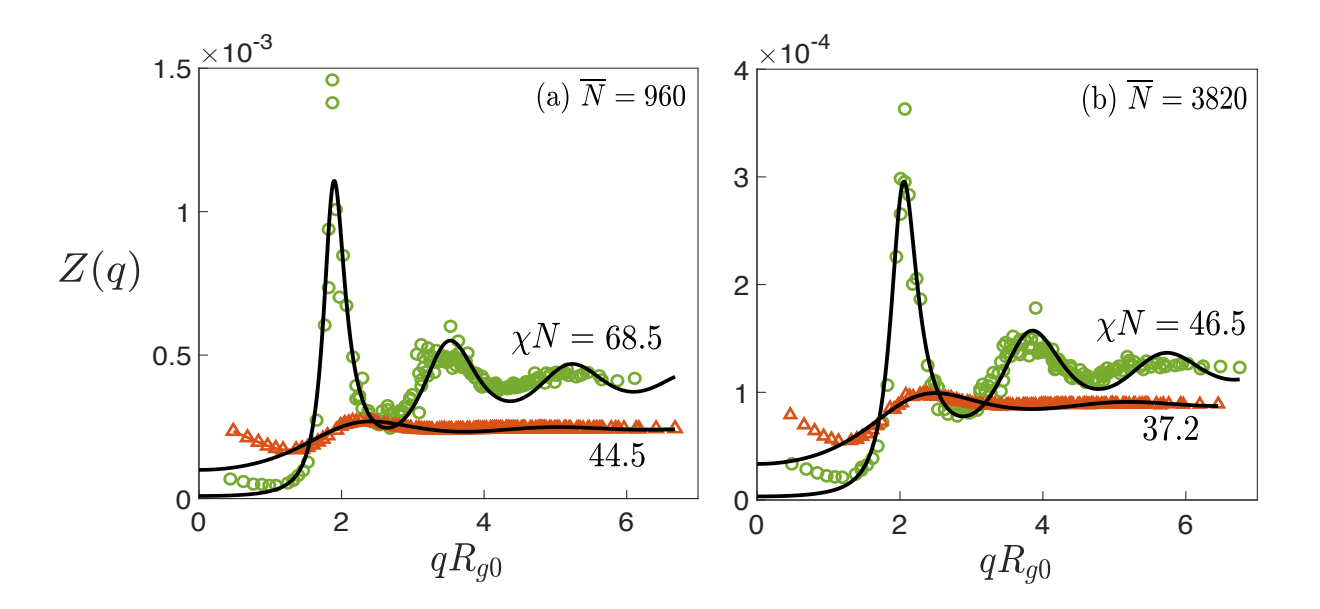


FIG. 5. Symbols show the calculated intermicellar correlations Z(q) at two values of χN for (a) $\overline{N} = 960$ and (b) $\overline{N} = 3820$. The solid lines in the plot are fits to the Percus-Yevick theory, in which the sphere radius, R_{hs} , an the effective volume fraction, η , and an overall constant of proportionality are adjusted to fit the data. The resulting fit parameters are in Table II. Note that a different ordinate scale is used for each \overline{N} .

results for Z(q) exhibit both a primary peak at a value of $qR_{g0} \simeq 2$ close to the value at which S(q) in Fig. 2 exhibits a primary maximum, and a secondary peak at a value of $qR_{g0} \sim 3.6$ to 3.8 similar to that at which S(q) shows a secondary shoulder. This confirms that the secondary shoulder in S(q) is indeed caused by the existence of a corresponding peak in Z(q), reflecting strong correlations in micelle positions, as suggested by previous analyses of scattering data [1–5]. The lower value of χN corresponds to a state relatively close to the CMT in which S(q) exhibits a primary peak but no secondary shoulder. The corresponding results for Z(q) are now nearly structureless, though S(q) still shows the single pronounced peak seen in Fig. 2 for lower values of χN . This indicates that at these lower values of $\chi N \sim (\chi N)_{\rm odt}^{\rm scf}$, S(q) probably cannot be correctly described by a model that attributes all scattering as originating from a liquid of spherical micelles.

TABLE II. Values of R_{hs}/Rg_0 , and η extracted from the fits of the intermicellar correlation Z(q) to the Percus-Yevick theory [20]. The data were fit to a prediction of the form $Z(q) = KZ_{PY}(qR_{hs}, \eta)$, where $Z_{PY}(qR_{hs}, \eta)$ denotes the Percus-Yevick prediction the structure factor of hard spheres of diameter R_{hs} and volume fraction η . The parameters K, R_{hs} and η are adjusted to fit the data.

\overline{N}	α	χN	R_{hs}/R_{g0}	η
960	2.5	44.5	1.228	0.1132
960	3.75	68.5	1.8098	0.4648
3820	7	37.2	1.1917	0.12414
3820	9	46.5	1.6503	0.44237

IV. CLUSTER POPULATION ANALYSIS

In this section, we characterize micelles in the disordered phase by analyzing results of the cluster analysis described in Section II. To begin this analysis, Fig. 6 depicts the fraction x_n of chains with aggregation number n for both models over a range of values of χN . At the higher invariant degree of polymerization (data reported previously [8]) x_n is a monotonically decreasing function of n for all values less than $(\chi N)_{\text{odt}}^{\text{sef}} = 36.6$ (measured values $\chi N \leq 34.8$) and develops a local maximum for all values greater than $(\chi N)_{\text{odt}}^{\text{sef}}$ (measured values $\chi N \geq 37.2$). This indicates emergence of proper micelles over a narrow range of values of χN near $(\chi N)_{\text{odt}}^{\text{sef}}$ [8]. Corresponding results for $\overline{N} = 960$ in Fig. 6 are qualitatively similar to those at $\overline{N} = 3820$. Here, x_n is still a monotonically decreasing function of n for $\chi N = 39.7$ and exhibits a weak maximum for $\chi N \geq 44.5$. The value of χN at the apparent CMT thus does appear to increase somewhat with decreasing \overline{N} , though the results for $\overline{N} = 3820$ suggest that the CMT rapidly approaches $(\chi N)_{\text{odt}}^{\text{sef}}$ with increasing \overline{N} for $\overline{N} > 10^3$.

Under conditions for which proper micelles exist, results of the cluster analysis can be used to quantify the fraction of free chains that remain outside of micelles. We apply this analysis only at values of χN for which x_n exhibits a local minimum and local maximum, and classify chains that belong to clusters of aggregation numbers less than the value of n

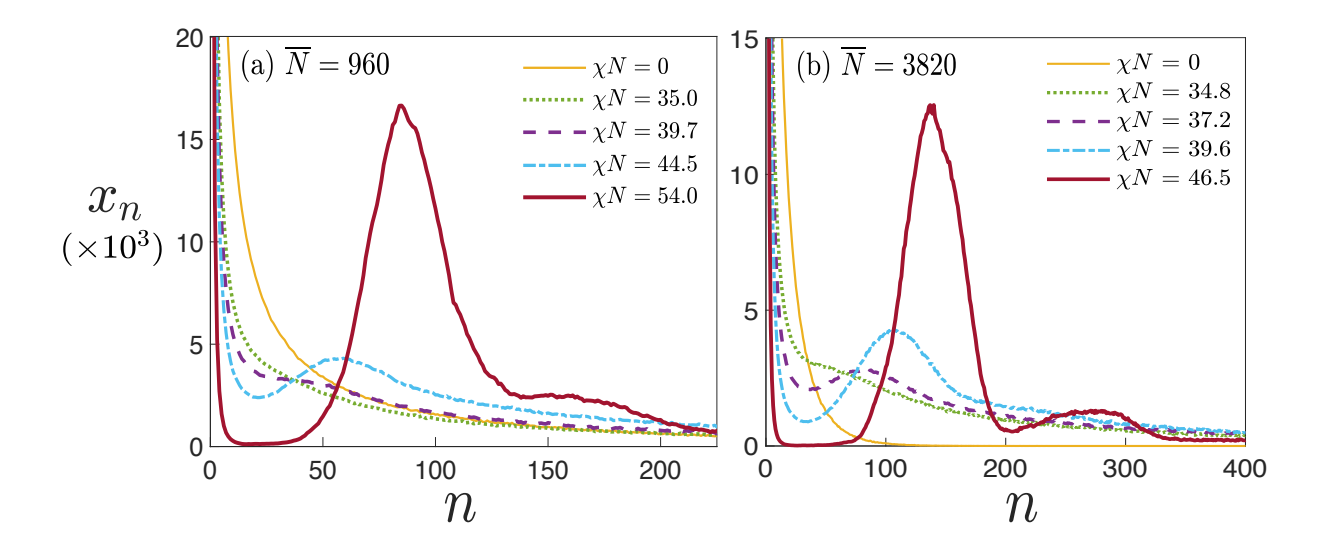


FIG. 6. Mole fraction x_n of chains that belong to clusters of aggregation number n for (a) $\overline{N} = 960$ and (b) $\overline{N} = 3820$. Note that the axis limits differ between panels. Panel (b) reproduced with permission from Ref. [8].

at the local minimum as "free" chains. Let x_{free} denote the total fraction of such chains, given by the sum of values of x_n from 1 to the value at which x_n is minimum.

Figure 7 shows simulation results for the fraction x_{free} where results from simulations of ordered BCC phases are used throughout the range of values of χN in which the ordered phase is found to remain stable (solid symbols), while results from disordered melts are used at lower values of χN (open symbols). For both values of \overline{N} , results from disordered and ordered phases form an apparently continuous line, indicating that crystallization has little if any effect on x_{free} . Moreover, x_{free} is substantial at the lowest value studied ($x_{\text{free}} \simeq 0.2$ to 0.4) and decreases with increasing χN . Figure 7 also compares simulation results to an SCFT prediction of x_{free} that we obtained by measuring the volume fraction of the minority monomer type at the midpoint between two neighboring micelles, and equating this to fx_{free} , with f=1/8. Agreement with this SCFT prediction is reasonably good at larger values of χN , particularly in light of differences between the definitions of x_{free} used in the cluster analysis and the SCFT analysis.

It is also illuminating to examine how the micelle aggregation numbers are influenced by χN and \overline{N} . To do so, we define n^* to be the value of n at which x_n is maximum. This quantity is estimated by fitting a region near the peak in x_n to a Gaussian function (using a region within $\pm 20\%$ of the maximum) and approximating n^* by the value of n at the maximum

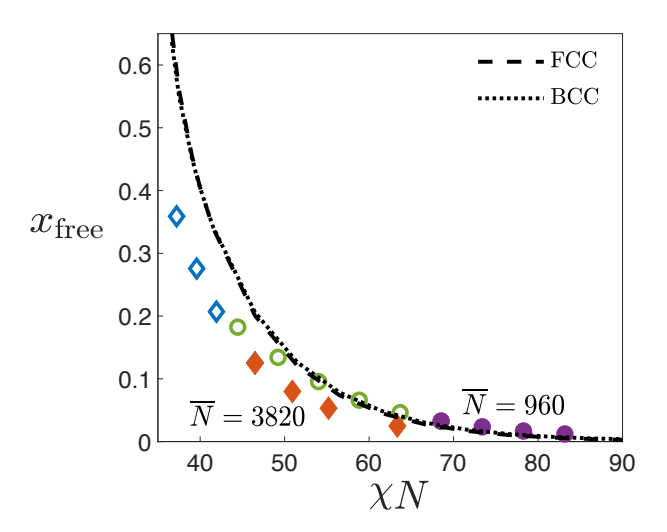


FIG. 7. Fraction of free chains x_{free} as a function of χN from simulations (symbols) and as predicted by SCFT. Diamonds and circles represent simulation results for $\overline{N} = 3820$ and $\overline{N} = 960$, respectively. Open and closed symbols represent results of simulations of disordered and ordered phases, respectively.

of that Gaussian. Figure 8 shows that n^* increases substantially with increasing χN in both ordered and disordered phases. Results for $\overline{N}=980$ show a statistically measurable difference in values of n^* from ordered and disordered phases at $\chi N=68.5$, the lowest value for which the ordered phase was found to remain stable. For $\overline{N}=3820$, the corresponding difference between values of n^* in the ordered and disordered phases is significantly smaller, and difficult to reliably measure because the difference (if any) is comparable to the scatter in our results for n^* . Results for n^* in the ordered phase are very sensitive to our choice of the number of molecules in the simulation [37].

SCFT predictions for n^* in crystalline structures, shown as lines in Fig. 8, were estimated as $n^* = m(1 - x_{\text{free}})$, where m is an SCFT prediction for the total number of molecules per micelle, and x_{free} is the SCFT prediction for the fraction of free chains, computed as described above. The SCFT prediction for m is computed by combining SCFT predictions for the optimal unit cell size with values of statistical segment length b and monomer concentration c appropriate to the simulation model (Table I). These predictions agree rather well with measurements of n^* in both the disordered and ordered micellar state.

While we have focused on the disordered liquid phase thus far, the cluster analysis may be applied in simulations of ordered micelle crystals as well. By way of example, Fig. 9

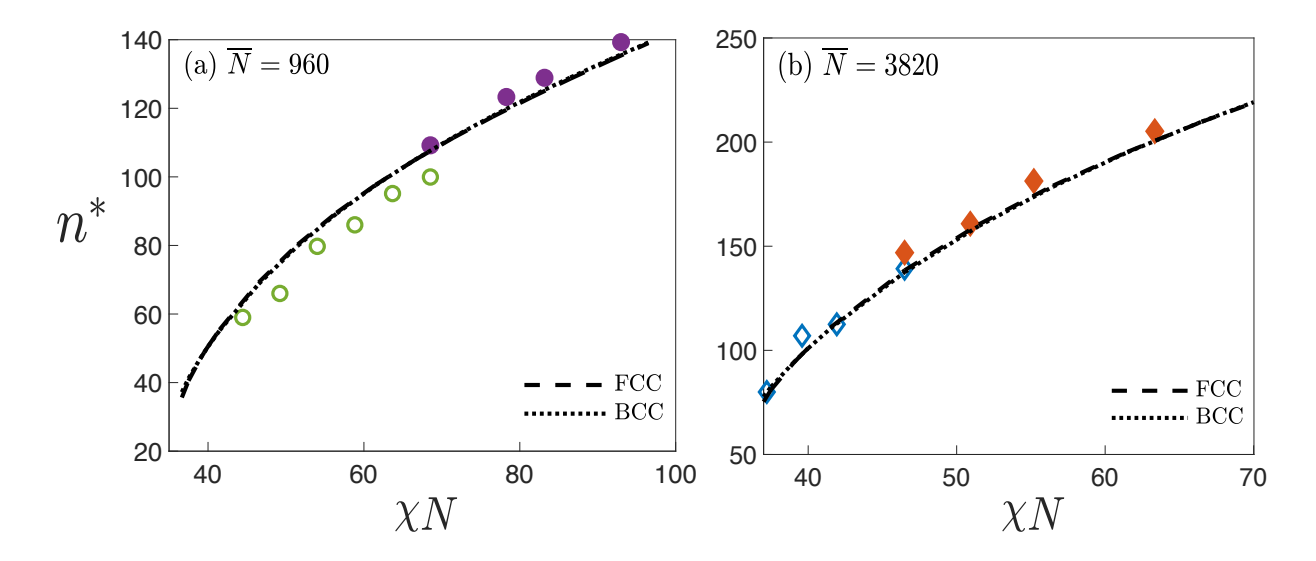


FIG. 8. Most probable micelle aggregation number n^* vs. χN for (a) $\overline{N} = 960$ and (b) $\overline{N} = 3820$. Results are shown only for values of χN for which x_n exhibits a local maximum. Open and closed symbols represent results obtained from simulations of disordered and ordered states, respectively. Results obtained from ordered states are shown for all values of χN for which the ordered state remained stable. Lines represent SCFT predictions for BCC and FCC crystals, which are visually indistinguishable on the scale of this plot. Note that the axis limits differ between panels.

provides the aggregation number fraction for a BCC crystal phase and the disordered liquid for $\overline{N}=960$ at $\chi N=68.5$. Interestingly, the cluster analysis clearly shows that micelles exhibit a polydispersity in the ordered phase as well as in the disordered phase: Note that the width of the primary peak in x_n in Fig. 9 is rather similar for both the ordered and disordered systems. Relative frequencies of micelles of different aggregation numbers can be related to corresponding differences in free energies of a hypothetical system containing one test micelle of constrained aggregation number in a fluctuating environment. The observation of similar polydispersities in crystal and liquid phases thus can be rationalized if we assume that the free energy differences associated with changes in aggregation number are controlled primarily by changes in intra-micellar free energy contributions rather than free energies arising from changes in the surrounding liquid or crystal of neighboring micelles that must be made to accommodate a change in the aggregation number of a test micelle. We expect these intra-micellar contributions, which arise primarily from changes in chain stretching and changes in the area of AB interface surrounding the core block of the test micelle, to be very similar in liquid and crystal phases.

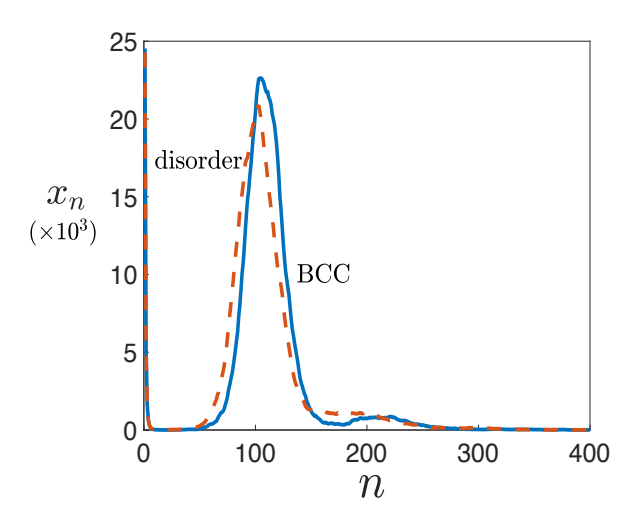


FIG. 9. Average mole fraction of chains x_n present in clusters of aggregation number n for $\overline{N} = 960$ at $\chi N = 68.5$ for the BCC phase (solid line) and the disordered phase (dashed line).

Returning our attention to the distributions for x_n in the disordered system in Fig. 6, we note that the data for $\overline{N} = 3820$ and $\chi N = 46.5$ exhibits a small second maximum at a value of n approximately twice that at which x_n exhibits a primary maximum. An analogous secondary feature is even more clearly visible in the cluster distribution for a BCC crystal shown in Fig. 9. We discuss the physical origin of this feature in the penultimate section of this paper, where we show that it arises from the formation of a small population of dimers consisting of two spherical micelles with connected cores regions.

V. MICELLE STRUCTURE

We focus in this section on analyzing the spatial structure of clusters with aggregation numbers within a range that corresponds to the main peak in the distribution for x_n , which we refer to here as micellar clusters. In well-segregated systems, for which the probability density for x_n exhibits a local minimum and a local maximum, we consider clusters for which n lies between the value at the local minimum and 1.6 times the value at the local maximum, as in our calculations of Z(q) and x_{free} . At lower values of χN , for which x_n decreases monotonically with n, we consider clusters with n in a range 20-140 for $\overline{N} = 960$ and 30-160 for $\overline{N} = 3820$. We then characterize the concentration profile of a micelle by considering how the average composition of the resulting population of clusters varies with

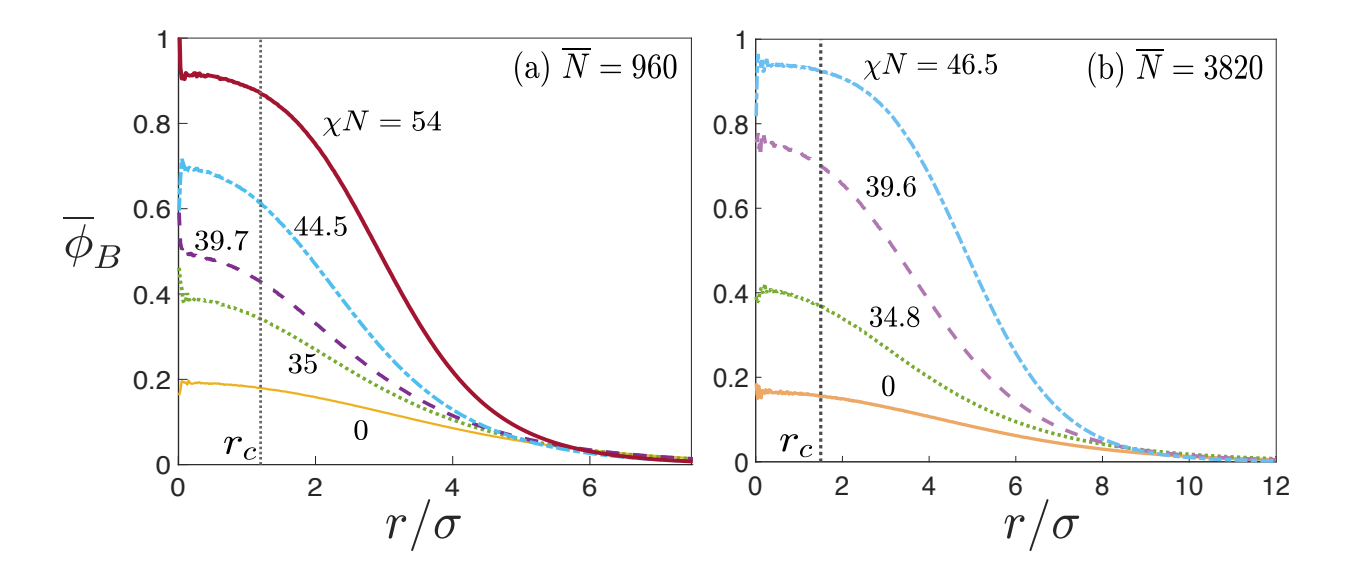


FIG. 10. Local volume fraction of the minority B-block as a function of the distance from the micelle center for different values of χN for (a) $\overline{N} = 960$ and (b) $\overline{N} = 3820$. The dotted vertical lines indicate the distances r_c used to compute the core volume fractions $\phi_B^{(c)}$. Note that the abscissa scales are different in the two panels. Panel (b) reproduced with permission from Ref. [8].

distance from the center of mass (COM) of the B (minority block) beads in each such cluster. We define the effective volume fraction ϕ_B of B beads within a region of volume ΔV as the ratio $\phi_B \equiv m_B/c\Delta V$, where m_B is the actual number of B beads in the region, and c is the monomer concentration (see Table I).

Let $\overline{\phi}_B(r)$ denote the average volume fraction of B beads at a distance r from the COM of a cluster. We compute this quantity from the average of ϕ_B over a thin spherical annular region of inner radius r around the COM of each cluster, averaged over time and over all micellar clusters that satisfy the above constraints on n [8]. Figure 10 shows the results of the calculation of $\overline{\phi}_B(r)$ in the disordered phase. In the analysis for $\overline{N}=3820$, which we reported previously [8], the observed value of $\overline{\phi}_B(r=0)$ at the micelle COM is found to be nonzero for all values of χN , but to increase particularly rapidly over a narrow range of values of χN centered around $(\chi N)_{\text{odt}}^{\text{scf}}=36.6$, and to saturate to values that approach unity at higher values of χN . Analogous behavior is seen here for $\overline{N}=960$, but the increase in $\overline{\phi}_B(r=0)$ is somewhat more gradual and occurs at somewhat higher values of χN .

At sufficiently low values of χN , for which x_n is a monotonically decreasing function, the clusters that are identified by our algorithm are not true micelles, but more diffuse

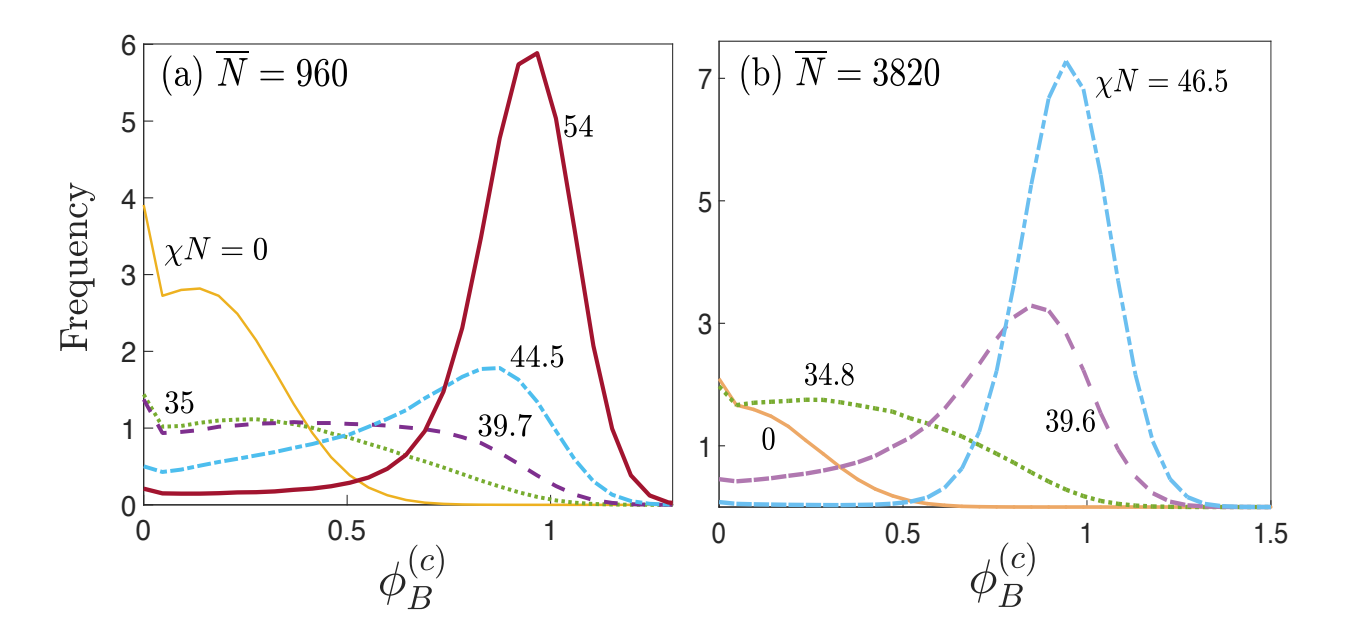


FIG. 11. Probability density for the minority block volume fraction in the micelle core at different values of χN for (a) $\overline{N} = 960$ and (b) $\overline{N} = 3820$. Note that the axis limits differ between the two panels. Panel (b) reproduced with permission from Ref. [8].

geometrical clusters that arise from random contacts between minority block beads. Our measurement of $\overline{\phi}_B(r)$ at values of χN comparable to $(\chi N)_{\rm odt}^{\rm scf}$ presumably includes contributions both from such diffuse clusters and from micelles with a more dense core region. To distinguish these two sub-populations, we have considered the probability distribution for the effective volume fraction ϕ_B within a small spherical region at the center of each cluster. We define $\phi_B^{(c)}$ to be the value of ϕ_B within a sphere of radius r_c of the cluster COM of mass, and use cutoff radii $r_c = 1.5\sigma$ for $\overline{N} = 3820$ and $r_c = 1.2\sigma$ for $\overline{N} = 960$; the values are indicated in Fig. 10 as vertical dotted lines. These values of r_c were chosen so as to be small enough to remain within the B-rich core region of a well segregated micelle, but large enough to contain many beads. Denoting ΔV as the volume of the core region, these choices for r_c furnish $c\Delta V = 21.7$ for $\overline{N} = 960$ and $c\Delta V = 21.2$ for $\overline{N} = 3820$ using the monomer concentrations c in Table I.

Figure 11 shows the calculated probability distributions of $\phi_B^{(c)}$. For $\overline{N}=960$, the most probable volume fraction is $\phi_B^{(c)}=0$ for $\chi N=0$ and 35, characteristic of diffuse clusters. At $\chi N=39.7$, we obtain a broad distribution of values of $\phi_B^{(c)}$, suggesting the co-existence of both diffuse and dense clusters at this value. At $\chi N \geq 44.5$, we see clear evidence of a

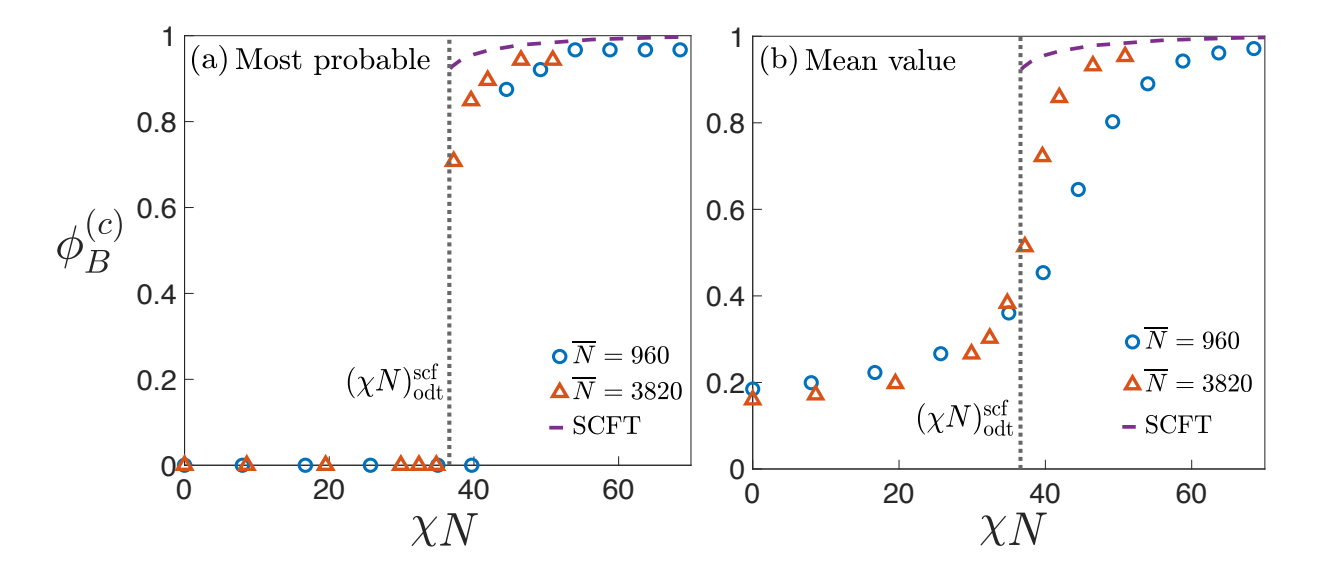


FIG. 12. Statistical characteristics of the minority component core volume fraction $\phi_B^{(c)}$. (a) Most probable value of $\phi_B^{(c)}$ for both models ($\overline{N}=960$ and $\overline{N}=3820$). (b) Mean value of $\phi_B^{(c)}$ for both models. In both plots, the vertical dotted line shows the SCFT ODT value (χN) $_{\rm odt}^{\rm scf}$, and the dashed purple line shows the SCFT prediction for the the average B volume fraction at the center of a micelle within a BCC crystal for $\chi N > (\chi N)_{\rm odt}^{\rm scf}$.

peak with a maximum at $\phi_B^{(c)} \simeq 1$, indicating the emergence of a new population of proper micelles with a core region that is nearly pure B. As shown in Fig. 11b, results for $\overline{N} = 3820$, which we reported previously [8], show the emergence of proper micelles at somewhat lower values of χN closer to $(\chi N)_{\rm odt}^{\rm scf}$.

To identify the emergence of micelles, Fig. 12 shows results for the most probable value of $\phi_B^{(c)}$ and its mean value as a function of χN . The results for $\overline{N}=3820$ have been reported previously [8]. The most probable value shows a discontinuous jump with increasing χN from a most probable value of $\phi_B^{(c)}=0$ at lower values of χN to a nonzero value comparable to unity at higher values. The value of χN at which the most probable value of $\phi_B^{(c)}$ becomes nonzero provides a simple estimate of the value of χN at the CMT [8]. The jump in the most probable value occurs very near $(\chi N)_{\text{odt}}^{\text{scf}}=36.6$ for $\overline{N}=3820$, but occurs at a slightly higher value of $\chi N\simeq 40-45$ for $\overline{N}=960$. The mean value of $\phi_B^{(c)}$, shown in Fig. 12b, shows a somewhat more smeared sigmoidal behavior centered around a higher value of χN for $\overline{N}=960$ than for $\overline{N}=3820$.

VI. MICELLE DIMERS

We now consider the interpretation of the secondary feature visible in Figs. 6 and 9, in which some plots of x_n show a secondary maximum at an aggregation number approximately twice that of value at which x_n is maximum. Figure 13 replots the data for x_n on a semilogarithmic scale, so as to emphasize this secondary feature. In each plot results for both ordered and disordered phases are shown at the lowest value of χN for which an initially ordered structure was found to remain stable ($\chi N = 68.5$ for $\overline{N} = 960$ and $\chi N = 46.5$ for $\overline{N} = 3820$). Results for ordered phases for both values of \overline{N} (dashed red lines) show the existence of multiple local maxima at values of n that are approximately equal to integer multiples of the value of n at first local maximum. Results obtained in the disordered phase (solid blue lines) differ with \overline{N} . Data for the higher $\overline{N} = 3820$ show a clear second local maximum at $n \simeq 2n^*$, whereas there is a shoulder for $\overline{N} = 960$. We show in what follows that clusters with $n \simeq 2n^*$ correspond primarily to pairs of spherical micelles with core blocks connected by threads or bridges of minority block material, each of which our cluster analysis algorithm identifies as a single larger cluster. Similarly, the higher order bumps in plots of x_n in the ordered phase correspond to groups of three or more micelles with core regions that are connected in a way that causes our algorithm to identify each as a single cluster. The more frequent formation of dimers in the BCC state can also serve as a mechanism for chain exchange, which could be connected to the more facile exchange kinetics in BCC packings of block polymer micelle solutions when compared to the disordered solution state [41].

Further information about micelle structure can be obtained by characterizing each micelle by a measure of shape anisotropy [42] as well as aggregation number. Let S denote a cluster gyration tensor, defined as a matrix with elements

$$S_{\alpha\beta} = \frac{1}{N} \sum_{i=1}^{N} r_{i\alpha} r_{i\beta} \quad , \tag{4}$$

where $r_{i\alpha}$ denotes Cartesian component α of the position of the i^{th} minority block (B) bead within a cluster, measured relative to the center-of-mass of the B beads in the cluster, and N is the number of such beads in the cluster. Let Δ denote the shape anisotropy defined as

$$\Delta = \frac{3}{2} \frac{\lambda_1^2 + \lambda_2^2 + \lambda_3^2}{(\lambda_1 + \lambda_2 + \lambda_3)^2} - \frac{1}{2} \quad , \tag{5}$$

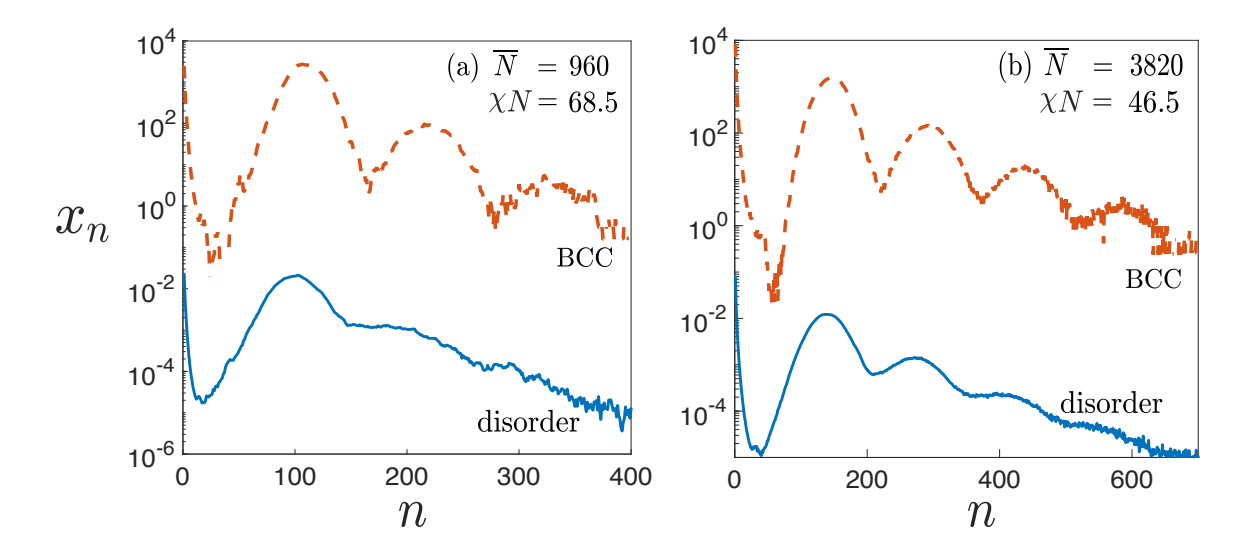


FIG. 13. Semilogarithmic plot of the mole fraction x_n of aggregation number n for the disordered phase (solid blue line) and ordered BCC phase (dashed red line). Results for the BCC phase are vertically shifted for clarity by multiplying x_n by 10^6 . Data for (a) $\overline{N} = 960$ are for $\chi N = 68.5$ and (b) data for $\overline{N} = 3820$ are at $\chi N = 46.5$. Note that the axis limits differ between panels.

where λ_1 , λ_2 , and λ_3 are the eigenvalues of the gyration tensor **S**. Note that $\Delta = 0$ for a spherically symmetric cluster, for which all three eignevalues are equal, and $\Delta \simeq 1$ for a rod-like cluster, for which one eigenvalue is much larger than the other two.

Figure 14 furnishes a heat map of the two-dimensional (2D) joint probability of finding a cluster with a specified pair of values of n and Δ in the ordered BCC phase at (i) $\chi N = 68.5$ for $\overline{N} = 960$ and (ii) $\chi N = 46.5$ for $\overline{N} = 3820$. Note that the primary maximum in each plot, corresponding to the main peak in a corresponding plot of x_n vs. n, is located at a small value of $\Delta < 0.1$, indicating that the peak around this maximum corresponds to a set of nearly spherical micelles. The secondary maximum in each plot appears at a value of n approximately twice that of the primary peak but now with a rather large shape anisotropy of $\Delta \simeq 0.7$. This secondary maximum, which corresponds to the second peak in x_n vs. n, thus arises from a population of much more anisotropic objects.

We now show that the secondary peak in these 2D plots arise from micelle dimers. The red star markers in both plots of Fig. 14 show the predicted values of Δ for an idealized model of a dimer consisting of two nearest neighbor micelles within a BCC lattice. The model used to compute this value consists of two spherical micelle cores with $\phi_B = 1$ within a region of radius R, separated by a distance X between the sphere centers. This model can

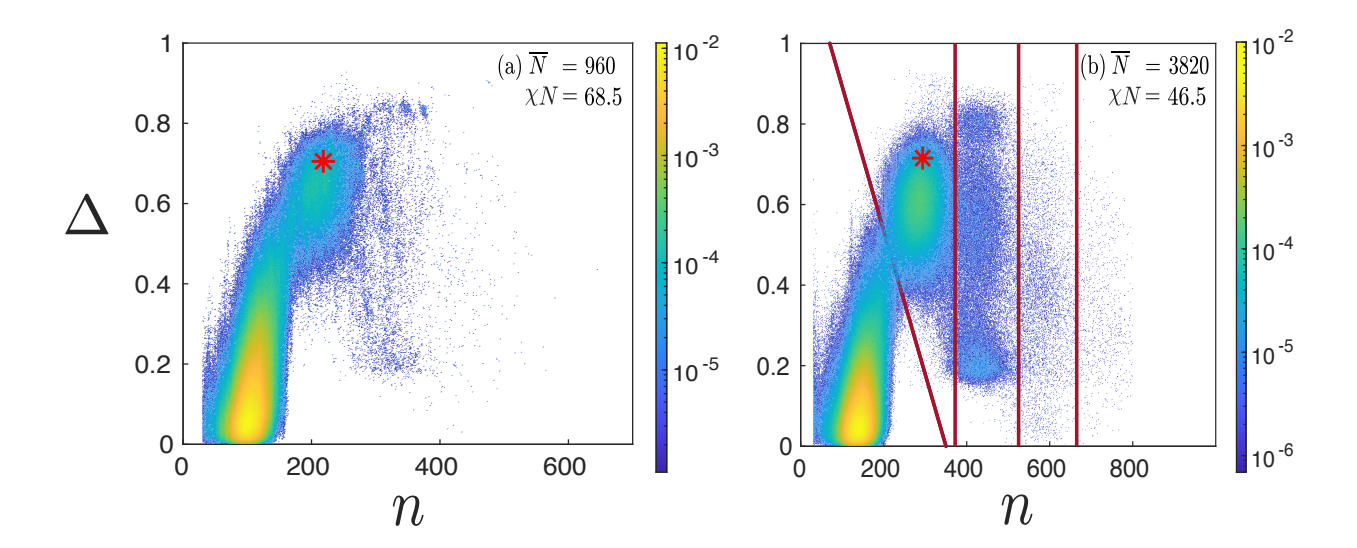


FIG. 14. Heat map for the joint probability density of specified aggregation number n and shape anisotropy Δ in simulations of the BCC ordered phase for (a) $\overline{N} = 960$ at $\chi N = 68.5$ and (b) $\overline{N} = 3820$ at $\chi N = 46.5$. The red star marker in each plot is the theoretically calculated shape anisotropy for a dimer of two micelles on nearest-neighbor lattice positions. Straight lines in (b) are boundaries of the regions used to divide clusters into individual micelle and micelle multiplets of different multiplicity. Note that the abscissa scales differ between panels.

be shown to yield

$$\Delta = \frac{3}{2} \frac{[0.4 + 2(X/2R)^2]^2 + 0.32}{[1.2 + 2(X/2R)^2]^2} - \frac{1}{2}$$
 (6)

To obtain the values shown in Fig. 14, the intermicelle distance X has been set equal to the distance between nearest neighbors in a perfect BCC lattice in the simulated unit cell, while the core radius R has been chosen so that the number $(4\pi R^3/3)c$ of monomers in each micelle core in the model corresponds to the number of B monomers in a micelle of aggregation number equal to the most probable aggregation number. The prediction of this idealized model is seen to be very close to the observed value of Δ at the secondary local maximum in the 2D histogram, confirming that this maximum corresponds to a population of nearest neighbor micelle dimers within a micelle crystal.

Red lines in Fig. 14b show boundaries that we have constructed to divide the population of all clusters within a simulation of an ordered BCC crystal into regions corresponding to nearly spherical micelle "unimers" (corresponding to the main peak in x_n vs. n), micelle dimers, trimers, and (rare) quadrimers. Dimers are aligned along {111} directions, producing a single peak in the heat map. There are three types of trimers in which the two end unimers

are at the corners of a cube and aligned along a {100}, {110}, or {111} direction relative to each other, producing the lobes in the trimer distribution.

To test the consistency of this classification scheme, we count the total number of micelles in the system, denoted by K, by counting each cluster in the unimer region of the 2D histogram as a single micelle, each cluster in the dimer region as two micelle, and so on for trimers and quadrimers. In a simulated system designed to accommodate a BCC lattice of 54 micelles, for $\overline{N} = 960$ and $\chi N = 78.3$, this scheme yields an average value $\overline{K} = 54$ with a very small standard deviation of 0.003 micelles, thereby confirming that the scheme correctly categorizes almost all clusters within such a crystal as either individual micelles or micelle multiplets. A similar classification was developed for all simulations of ordered phases for both models, and verified using the same methodology.

Using this classification scheme, we can unambiguously count the number of bridges between nearest-neighbor micelles within a BCC crystal, and the fraction of all possible nearest-neighbor "bonds" within a BCC crystal along which there are such bridges between micelles. This fraction was less than 0.02 (i.e., less than 2%) for all the cases considered here, and decreases with increasing χN .

We have performed a similar analysis for the disordered state in Fig. 15, using the same values of χN as in Fig. 14. The structure in the disordered phase is qualitatively similar to that in the ordered phase. In the disordered phase, however, the main and secondary peaks are less well separated, suggesting a somewhat greater tendency for micelles to form elongated objects of intermediate aggregation number in addition to simple micelle "dimers".

We next consider the geometrical structure of a population of clusters formed from micelle dimers. For this purpose, it is useful to use the eigenvectors of the gyration tensor S to define a coordinate system for each cluster. In an idealized model of the minority beads of a dimer as a dumbbell consisting of two connected spheres, the eigenvector of S associated with its largest eigenvector would lie along the axis connecting the centers of the spheres. To characterize real clusters, we thus define a coordinate z for each S bead given by the distance projection of its position relative to the cluster center-of-mass onto the eigenvector of S associated with the largest eigenvalue. Given a population of clusters generated by a simulation, we then can compute a histogram of values of z for all S monomers belonging to molecules in each cluster, and use this histogram to create a one dimensional density $\rho(z)$ at each value of z, defined such that $\int dz \rho(z)$ is the average number of S monomers

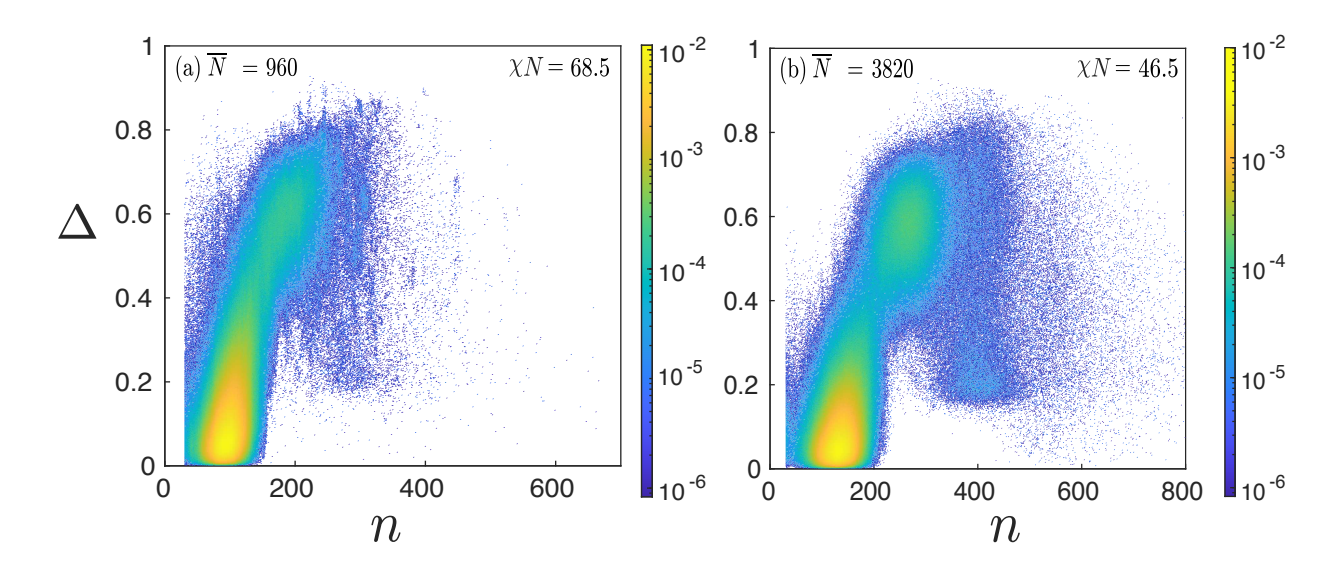


FIG. 15. Heat map for the frequency of observing shape anisotropy Δ and aggregation number n, similar to Fig. 14, but now for the disordered phase for (a) $\overline{N} = 960$ at $\chi N = 68.5$ and (b) $\overline{N} = 3820$ at $\chi N = 46.5$. Note that the abscissa scales differ between panels.

per cluster. We then define an effective radius $r_{\rm eff}(z)$ at each value of z to be the radius of a hypothetical cylindrically symmetric object of monomer concentration c that would give the same one-dimensional density $\rho(z)$ as that measured in the simulation, such that $\rho(z) = c\pi r_{\rm eff}^2$, where c is the average total monomer concentration in the simulation model (Table I).

In our analysis of $r_{\rm eff}(z)$, it proves important to take into account that micelle dimers and other multiplets are transient structures that are constantly formed when new bridges are formed between nearby micelles and destroyed when bridges break. An analysis of the dynamics of these processes is given in the Supplemental Material [37]. We find that a significant fraction of dimers are very short-lived structures that break apart in less than 1000 molecular dynamics time steps. There is, however, also smaller fraction that is stable for thousands of time steps. In our analysis of structure, we present separate results for short lived and long-lived dimers within a BCC crystal. For this purpose, we classify a dimer as long-lived if it survived for at least 1000 timesteps, and short-lived if it survived for less than 1000 steps.

The values of the effective radius r_{eff} as a function of position z along the main axis of the dimers within a BCC crystal appears in Fig. 16. Results are plotted as functions of a normalized coordinate $2z/r_0$ in which r_0 is the distance between nearest-neighbor lattice

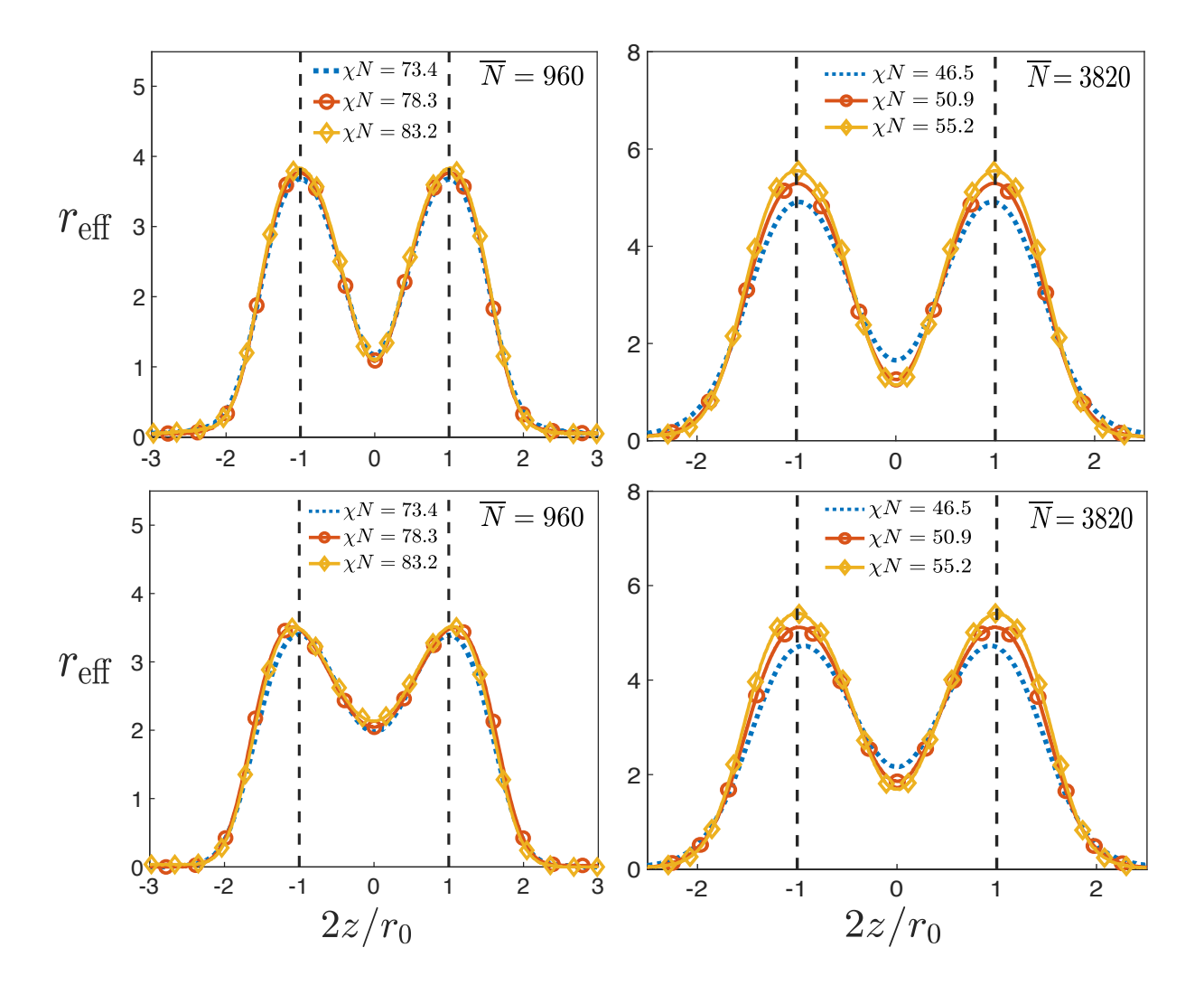


FIG. 16. Short lived (top row) and long lived (bottom row) micelle dimer profiles showing the variation in an effective radius $r_{\rm eff}$ vs. the distance z from the center of the micelle dimer. z is normalized by $r_0/2$ where r_0 is the distance between the nearest neighboring micelles in a BCC crystal with a unit cell length of L/3 where L is the simulation box length. $r_{\rm eff}$ is given in simulation units, in which the range σ of the pair interaction is set to unity. Note that the axis limits differ between panels.

points in a perfect $3 \times 3 \times 3$ BCC crystal constructed within the simulation unit cell. In a simplified model of a dimer as two connected spheres, this would yield $2z/r_0 = \pm 1$ at the centers of the spheres. The value of $r_{\rm eff}$ at the local maxima that occur at approximately these values thus correspond approximately to the radii of the micelle cores. The fact that $r_{\rm eff}(z)$ exhibits local maxima very close to $2z/r_0 = \pm 1$ indicates that connected micelles within a BCC crystal remain very close to their ideal lattice positions. Each plot of $r_{\rm eff}(z)$

vs. z also shows a local minimum at z=0. The value at this local minimum is a measure of the radius of the bridge of B monomers that connects the two micelle cores. The fact that all of these plots show a distinct minimum confirms that these are clusters do indeed all have a dimer or "dumbbell" shape with mass concentrated near the two ends, rather than a more uniform rodlike distribution. The ratio of the the bridge radius to micelle core radius ranges from 0.2 to 0.3 for short-lived dimers and and 0.4 to 0.55 for the long-lived dimers. The bridges between micelles appear to be thick enough to be visualized as bridges formed by the core blocks of multiple molecules, rather than more tenuous single-molecule bridges, particularly for the long-lived dimers.

VII. SUMMARY

The present contribution builds substantially on our preliminary communication on simulations of disordered asymmetric diblock copolymer melts [8], which focused solely on a limited analysis of the results obtained at the higher invariant degree of polymerization $\overline{N} = 3820$ available from Model S2-64. Here, we have investigated for those same properties at an even more experimentally-relevant value of $\overline{N} = 960$ using Model S1-64, and we have provided additional information on the structure, dynamics and thermodynamics for both values of \overline{N} . In this final section, we summarize the key outcomes of our analysis of the simulation data and their implications for experiments and theory.

Overall, the results presented here support the picture of the disordered micelle state described in our prior work [8]. Explicitly, we found previously [8] for $\overline{N} = 3820$ that there exists (i) a shoulder in S(q) as χN increases in the disordered state that is not predicted by the RPA (Fig. 2); (ii) a systematic deviation from the linear dependence of $S^{-1}(q)$ that is roughly coincident with the ODT predicted by SCFT but without the sudden decrease of $S^{-1}(q)$ that would accompany an order-disorder transition (Fig. 3); and (iii) a clear emergence of a population of a peak in the average mole fraction of chains with aggregation number n above the SCFT ODT (Fig. 6) where the nearly spherical micelles have cores that are almost pure (Figs. 11 and 12). Taken together, these data support a model where the CMT is roughly coincident with the ODT predicted by SCFT [8], with the true ODT taking place at a higher value of χN .

Inspection of Figs. 2, 3, 6, 11 and 12 shows that the picture we developed previously [8] at

 $\overline{N}=3820$ holds for the substantially lower value of $\overline{N}=960$ investigated here, albeit with smaller aggregation numbers and larger values of χN at $\overline{N} = 960$ required to produce the phenomena seen at $\overline{N} = 3820$. The most notable effects of \overline{N} are qualitative differences in the structure factor near the SCFT ODT. Namely, results for the system with a larger value of $\overline{N}=3820$ exhibit a weak inflection at $\chi N\simeq (\chi N)_{\mathrm{odt}}^{\mathrm{scf}}$ in a plot of $S^{-1}(q^*)$ vs. χN . The analogous plot for the system with a smaller value of $\overline{N} = 960$ does not, however, exhibit such an inflection, and instead exhibits behavior qualitatively similar to that observed in studies of more nearly symmetric copolymers [26, 28, 40]. We assume that the inflection in this plot would become sharper for systems of even greater \overline{N} , approaching a discontinuous jump in the limit $\overline{N} \to \infty$, but that it is washed out in systems of modest \overline{N} for which both the appearance of micelles and the build-up of correlations in micelle position is found to occur over a wider range of values of χN . The appearance of an inflection in a plot of $S^{-1}(q^*)$ vs. χN (or, equivalently, inverse temperature 1/T) thus seems to provide a reliable signature of the CMT only in systems with very large values of N. Overall, our results confirm the existence of a crossover from molecularly disordered regime to a liquid of micelles with increasing χN , and suggest that, with increasing N, the crossover occurs over an increasingly narrow range of values of χN centered around a value that rapidly approaches $(\chi N)_{\text{odt}}^{\text{scf}}$, in qualitative agreement with earlier theoretical predictions [33, 34].

In addition to the approaches used in our prior work [8] to identify the onset of the disordered micellar liquid, we have developed new evidence here by analyzing the structure factor in the context of the Percus-Yevick theory [20] in Fig. 5, which has impact on analyses of scattering data in experiments. The peaks in the intermicellar correlations Z(q) occur at the same wavenumbers q of the corresponding features in the structure factor S(q). This correspondence between features in Z(q) and S(q) is largely independent of \overline{N} . Our analysis of Z(q) shows, however, that micelles are present at significantly lower values of χN than those at which this feature becomes visible, because correlations in micelle positions remain rather weak near the CMT. Analysis of both S(q) and Z(q) also clearly shows that the strength of correlations among micelle positions increases more rapidly with increasing χN in systems of greater \overline{N} . Observation of this secondary feature in S(q) thus indicates the existence of a correlated liquid of micelles, but is not a sufficiently sensitive indicator to be used to identify the CMT.

Our analysis of the primary peak in the structure factor (Fig. 4), the derivative of the

free energy with χN [37], the fraction of free chains (Fig. 7), and the most probable micelle aggregation numer (Fig. 8) show that predictions from SCFT for ordered BCC structures provides remarkably good estimates for these properties in the disordered micellar liquid. These results support prior work [29, 30, 32] comparing SCFT predictions to simulations of disordered diblock copolymer melts. Unfortunately, we were unable to determine definitively how much the true ODT in our simulations deviates from the SCFT prediction; initially ordered systems spontaneously melt at sufficiently low χN , but initially ordered systems fail to crystallize in our simulations. The lower bounds on $(\chi N)_{\rm odt}$ obtained here [37] are, however, enough to show that the difference $(\chi N)_{\rm odt} - (\chi N)_{\rm odt}^{\rm scf}$ between values of χN at the actual and SCFT predictions for the order-disorder transition is substantially greater than the difference between the value at the CMT and the predicted SCFT transition. If we tentatively treat these lower bounds as the best available estimates of $(\chi N)_{\rm odt}$, the results suggest that $(\chi N)_{\rm odt}$ increases rather rapidly with decreasing \overline{N} in the experimentally relevant range of values.

The cluster analysis presented here shows the existence of a small but easily measurable population of micelle dimers at conditions near the order-disorder transition. Evidence of dimers was found in both ordered and disordered phases, but the analysis and evidence are particularly clear in the ordered phase. Analysis of dynamics in the ordered phase, discussed in the Supplemental Material [37], showed frequent formation and rapid destruction of bridges between the core blocks of nearest-neighbor micelles. The presence of these short-lived dimers is not expected to affect most experimentally accessible properties, but drew our attention in part because we found that it complicates attempts to use our cluster analysis to characterize dynamics in these systems by identifying elementary dynamical processes such as unimer insertion and expulsion and micelle fission or fusion. We anticipate that the dynamics of the disordered micelle liquid will be a fruitful avenue for future work.

ACKNOWLEDGMENTS

This work was supported primarily by NSF grant DMR-1719692, using computational resources provided by the Minnesota Supercomputing Institute (MSI) at the University of Minnesota. Part of this work was carried out with equipment supported by funding from the National Science Foundation through the UMN MRSEC under Award Number DMR-

- [1] D. Kinning and E. Thomas, Hard-sphere interactions between spherical domains in diblock copolymers, Macromolecules 17, 1712 (1984).
- [2] M. Schwab and B. Stühn, Thermotropic transition from a state of liquid order to a macrolattice in asymmetric diblock copolymers, Phys. Rev. Lett. **76**, 924 (1996).
- [3] M. Schwab and B. Stühn, Asymmetric diblock copolmers phase behavior and kinetics of structure formation, Colloid Polym. Sci. **275**, 341 (1997).
- [4] J. Adams, D. Quiram, W. Graessley, R. Register, and G. Marchand, Ordering dynamics of compositionally asymmetric styrene-isoprene block copolymers, Macromolecules 29, 6026 (1996).
- [5] X. Wang, E. E. Dormidontova, and T. P. Lodge, The order-disorder transition and the disordered micelle regime for poly(ethylenepropylene-b-dimethylsiloxane) spheres, Macromolecules 35, 9687 (2002).
- [6] J. K. Kim, H. H. Lee, S. Sakurai, S. Aid, J. Masomoto, S. Nomura, Y. Kitagawa, and Y. Suda, Lattice disordering domain dissolution transitions in polystyrene-block-poly(ethylene-co-but-1-ene)-block-polystyrene triblock copolymers having a highly asymmetric composition, Macromolecules 32, 6707 (1999).
- [7] C. D. Han, N. Y. Vaidya, D. Kim, G. Shin, D. Yamaguchi, and T. Hashimoto, Lattice disordering/ordering and demicellization/micellization transitions in highly asymmetric polystyreneblock-polyisoprene copolymers, Macromolecules 33, 3767 (2000).
- [8] A. Chawla, F. S. Bates, K. D. Dorfman, and D. C. Morse, Identifying a critical micelle temperature in simulations of disordered asymmetric diblock copolymers, Phys. Rev. Mater. 5, L092601 (2021).
- [9] G. Ungar, Y. Liu, X. Zeng, V. Percec, and W.-D. Cho, Giant supramolecular liquid crystal lattice, Science **299**, 1208 (2003).
- [10] X. Zeng, G. Ungar, Y. Liu, V. Percec, A. E. Dulcey, and J. K. Hobbs, Supramolecular dendritic liquid quasicrystals, Nature 428, 157 (2004).
- [11] S. Lee, M. J. Bluemle, and F. S. Bates, Discovery of a Frank-Kasper σ phase in sphere-forming block copolymer melts., Science **330**, 349 (2010).

- [12] M. Huang, C.-H. Hsu, J. Wang, S. Mei, X. Dong, Y. Li, M. Li, H. Liu, W. Zhang, T. Aida, W.-B. Zhang, K. Yue, and S. Z. Cheng, Selective assemblies of giant tetrahedra via precisely controlled positional interactions, Science 348, 424 (2015).
- [13] K. Yue, M. Huang, R. L. Marson, J. He, J. Huang, Z. Zhou, J. Wang, C. Liu, X. Yan, K. Wu, Z. Guo, H. Liu, W. B. Zhang, P. Ni, C. Wesdemiotis, W. B. Zhang, S. C. Glotzer, and S. Z. Cheng, Geometry induced sequence of nanoscale Frank-Kasper and quasicrystal mesophases in giant surfactants, Proc. Natl. Acad. Sci. USA 113, 14195 (2016).
- [14] K. Kim, M. W. Schulze, A. Arora, R. M. Lewis III, A. Hillmyer, K. D. Dorfman, and F. S. Bates, Thermal processing of diblock copolymer melts mimics metallurgy, Science 356, 520 (2017).
- [15] S. A. Kim, K. J. Jeong, A. Yethiraj, M. K. Mahanthappa, J. Jeong, A. Yethiraj, and M. K. Mahanthappa, Low-symmetry sphere packings of simple surfactant micelles induced by ionic sphericity, Proc. Natl. Acad. Sci. USA 114, 4072 (2017).
- [16] C. M. Baez-Cotto and M. K. Mahanthappa, Micellar Mimicry of Intermetallic C14 and C15 Laves Phases by Aqueous Lyotropic Self-Assembly, ACS Nano 12, 3226 (2018).
- [17] Z. Su, C.-h. Hsu, Z. Gong, X. Feng, J. Huang, R. Zhang, Y. Wang, J. Mao, C. Wesdemiotis, T. Li, S. Seifert, W. Zhang, T. Aida, M. Huang, and S. Z. D. Cheng, Identification of a Frank-Kasper Z phase from shape amphiphile self-assembly, Nat. Chem. 11, 899 (2019).
- [18] M. W. Bates, J. Lequieu, S. M. Barbon, R. M. Lewis III, K. T. Delaney, A. Anastasaki, C. J. Hawker, G. H. Fredrickson, and C. M. Bates, Stability of the A15 phase in diblock copolymer melts, Proc. Natl. Acad. Sci. USA 116, 13194 (2019).
- [19] K. D. Dorfman, Frank-Kasper phases in block copolymers, Macromolecules 54, 10251 (2021).
- [20] J. K. Percus and G. J. Yevick, Analysis of classical statistical mechanics by means of collective coordinates, Phys. Rev. 100, 1 (1958).
- [21] S. Lee, C. Leighton, and F. S. Bates, Sphericity and symmetry breaking in the formation of Frank-Kasper phases from one component materials, Proc. Natl. Acad. Sci. USA 111, 17723 (2014).
- [22] M. W. Matsen and M. Schick, Stable and unstable phases of a diblock copolymer melt, Phys. Rev. Lett. 72, 2660 (1994).
- [23] G. H. Fredrickson and E. Helfand, Fluctuation effects in the theory of microphase separation in block copolymers, J. Chem. Phys. 87, 697 (1987).

- [24] P. Grzywacz, J. Qin, and D. C. Morse, Renormalization of the one-loop theory of fluctuations in polymer blends and diblock copolymer melts, Phys. Rev. E **76**, 061802 (2007).
- [25] J. Qin, P. Grzywacz, and D. C. Morse, Renormalized one-loop theory of correlations in diblock copolymers, J. Chem. Phys. 135, 084902 (2011).
- [26] J. Qin and D. C. Morse, Fluctuations in symmetric diblock copolymer melts: Testing theories old and new, Phys. Rev. Lett. **108**, 238301 (2012).
- [27] J. Glaser, J. Qin, P. Medapuram, M. Müller, and D. Morse, Test of a scaling hypothesis for the structure factor of disordered diblock copolymer melts, Soft Matter 8, 11310 (2012).
- [28] J. Glaser, J. Qin, P. Medapuram, and D. C. Morse, Collective and Single-Chain Correlations in Disordered Melts of Symmetric Diblock Copolymers: Quantitative Comparison of Simulations and Theory, Macromolecules 47, 851 (2014).
- [29] J. Glaser, P. Medapuram, T. M. Beardsley, M. W. Matsen, and D. C. Morse, Universality of block copolymer melts, Phys. Rev. Lett. 113, 068302 (2014).
- [30] P. Medapuram, J. Glaser, and D. C. Morse, Universal phenomenology of symmetric diblock copolymers near the order–disorder transition, Macromolecules 48, 819 (2015).
- [31] T. Ghasimakbari and D. C. Morse, Correlations in disordered melts of asymmetric diblock copolymers, Macromolecules **51**, 2335 (2018).
- [32] T. Ghasimakbari and D. C. Morse, Order-disorder transitions and free energies in asymmetric diblock copolymers, Macromolecules **53**, 7399 (2020).
- [33] J. Wang, Z.-G. Wang, and Y. Yang, Nature of disordered micelles in sphere-forming block copolymer melts, Macromolecules 38, 1979 (2005).
- [34] E. E. Dormidontova and T. P. Lodge, The order-disorder transition and the disordered micelle regime in sphere-forming block copolymer melts, Macromolecules **34**, 9143 (2001).
- [35] A. Semenov, Contribution to the theory of microphase layering in block-copolymer melts, Sov. Phys. JETP **1256**, 733 (1985).
- [36] A. Semenov, Microphase separation in diblock-copolymer melts: ordering of micelles, Macromolecules 22, 2849 (1989).
- [37] See Supplemental Material at [URL will be inserted by publisher] for further details of MD simulations, analysis of the structure factor, thermodynamic analysis, micelle dimer dynamics and dimer structure.
- [38] J. A. Mysona, A. V. McCormick, and D. C. Morse, Simulation of diblock copolymer surfac-

- tants. I. Micelle free energies, Phys. Rev. E 100, 012602 (2019).
- [39] L. Leibler, Theory of microphase separation in block copolymers, Macromolecules **13**, 1602 (1980).
- [40] F. Bates, J. Rosedale, and G. Fredrickson, Fluctuation effects in a symmetric diblock copolymer near the order-disorder transition, J. Chem. Phys. **92**, 6255 (1990).
- [41] S. H. Choi, F. S. Bates, and T. P. Lodge, Molecular exchange in ordered diblock copolymer micelles, Macromolecules 44, 3594 (2011).
- [42] D. N. Theodorou and U. W. Suter, Shape of unperturbed linear polymers: polypropylene, Macromolecules 18, 1206 (1985).

Supplemental Material for "Simulations of sphere-forming diblock copolymer melts"

Anshul Chawla, Frank S. Bates, Kevin D. Dorfman,* and David C. Morse[†]

Department of Chemical Engineering and Materials Science,

University of Minnesota, 421 Washington Ave. SE, Minneapolis, MN 55455, USA

CONTENTS

I. Overview	2
II. Simulation system sizes	3
A. Disordered phase	3
B. Spontaneous melting and crystallization	6
III. Structure factor	8
IV. Phase Transitions and Thermodynamics	10
A. Order-Disorder Transition Temperature	10
B. Free Energy	11
C. Latent Heat	12
V. Dynamics of inter-micelle bridges	15
A. Mathematical model	15
B. Results	17
References	19

I. OVERVIEW

This supplemental material discusses technical details of the design and analysis of the molecular dynamics (MD) simulations presented in the associated article. All simulations were constant temperature, constant pressure (NPT) simulations of simple bead-spring models that were used in previous work [1–4] on symmetric and modestly asymmetric diblock copolymers. These simulations were performed with the Hoomd-blue simulation package [5, 6], using Martyna-Tuckerman-Tobias-Klein barostat-thermostat to control temperature and pressure [7, 8]. We use a timestep of 0.005 in natural simulation units, $\sigma/\sqrt{k_BT/m}$, where σ is the range of the non-bonded pair interaction and m is bead mass. Simulations reported here were performed using models S1-64 ($\overline{N}=960$) and S2-64 ($\overline{N}=3820$), for chains containing a minority block of 8 beads and a majority block of 56 beads. Each model

^{*} dorfman@umn.edu

 $^{^{\}dagger}$ morse012@umn.edu

was simulated over a range of value of a control parameter $\alpha = (\epsilon_{AB} - \epsilon_{AA})/k_BT$, with fixed values for all other parameters, as discussed in the main text. The calibration of the relationship between α and χ determined for each model in previous work was used to estimate values of χN for each simulation.

II. SIMULATION SYSTEM SIZES

The number of molecules used for each simulation, denoted by M, was generally chosen so as to yield a simulation cell with average dimensions that are at least approximately commensurate with the preferred unit cell of a hypothetical body-centered-cubic unit (BCC) crystal phase. All simulations were performed using an $L \times L \times L$ cubic simulation unit cell in which L fluctuates slightly under control of a barostat. Most simulations were designed to accommodate a $3 \times 3 \times 3$ array of cubic unit unit cells (54 micelles), though a smaller number of simulations were designed to accommodate a $2 \times 2 \times 2$ array (16 micelles). For each simulation a value for M was computed by taking $M = cL^3/N$, where L is the intended simulation cell size, N = 64 is the number of monomers per chain, and c is nominal monomer density for infinite homopolymers in the model of interest (i.e., $c = 3\sigma^{-3}$ for model S1 and $c = 1.5\sigma^{-3}$ for model S2), and rounding M to the nearest integer.

In most cases, values of L were chosen such that the wavenumber associated with the primary Bragg scattering peak of the intended BCC crystal arrangement would be equal to an estimate or measurement of the wavenumber q^* at which S(q) is maximum in the disordered phase. Somewhat different procedures for estimating q^* were used for simulations that were designed primarily to study properties of the disordered phase than for simulations that were designed to study spontaneous melting and crystallization, with greater care taken for simulations that were designed to study spontaneous melting and crystallization.

A. Disordered phase

All simulations that were used primarily to study properties of the disordered phase were designed to accommodate a $3 \times 3 \times 3$ array of BCC unit cells, giving a crystal of 54 micelles.

In all simulations of either model for which $\chi N < (\chi N)_{\rm odt}^{\rm scf}$, a value of L was chosen such that the primary peak of the ordered phase would be commensurate with a peak wavenumber

 q^* predicted from the Random Phase Approximation (RPA).

For simulations of model S1-64 for which $\chi N > (\chi N)_{\rm odt}^{\rm scf}$, simulations of systems with increasing values of χN were performed sequentially, using the results of previous simulations to estimate an extrapolated value of q^* for each new, higher value. For $(\chi N)_{\rm odt}^{\rm scf} < \chi N \le 68.5$, measured values of q^* from each simulation were used to predict the next higher value, which was used to choose a value of M for the simulation. The measured values of q^* for the disordered phase at $\chi N \le 68.5$ were then extrapolated to predict values of q^* and choose corresponding values of M for the three highest values of $\chi N = 73.4, 78.3$, and 83.2.

Two different strategies were used to choose value of M for simulations of model S2-64 in systems with $(\chi N) > (\chi N)_{\text{odt}}^{\text{scf}}$. For simulations with $\chi N = 37.2, 39.6$, and 41.9 the simulation box length L was chosen to be three times the SCFT prediction of the corresponding BCC unit cell. For $\chi N = 46.5, 50.9$, and $\chi N = 55.2$, M was chosen using estimated values of q^* obtained by extrapolating from values of q^* measured at lower values of χN .

Table S1 lists values of α , χN , M and other parameters for simulations of the disordered phases of models S1-64 and model S2-64, respectively.

A variety of strategies were used to choose values of M in simulations of the disordered phase, in part, because we were simultaneously gathering initial data and refining our procedures for choosing M over the course of this research. Comparisons of a few pairs of simulations of model S2-64 that were performed with equal values of α but different values of M showed that results for S(q) and other properties of the disordered phase in a $3 \times 3 \times 3$ system were quite insensitive to changes in the choice of value for M, particularly at values of χN less than or slightly greater than $(\chi N)_{\text{odt}}^{\text{sef}}$. This observation motivated our decision use the simple RPA prediction for q^* in systems with $\chi N < (\chi N)_{\text{odt}}^{\text{sef}}$ for both models and to not rerun early simulations of model S2-64 that were designed using SCFT predictions to estimate q^* , which we considered less accurate than methods based on extrapolation of measured values of q^* . Any dependence of results for properties of the disordered phase on slight changes in M would in any case indicate the presence of a finite size artifact. The free energy of the ordered phase is, however, quite sensitive to the choice of a value for M, since M controls the unit cell size in a nearly incompressible liquid.

TABLE S1: Simulation parameters for disordered phase simulations where M is the number of chains having a length N=64, $N_{\rm step}$ is the length of the simulation (in timesteps) after initial equilibration. The table shows parameters used for both a) model S1-64 and b) model S2-64. Horizontal lines separate the simulations according to the strategy used to choose a value for M. The first group in model S1-64 is designed to be commensurate with the RPA prediction of q^* . The second group are simulations that were performed sequentially in order of increasing α , using results from each simulation to extrapolate a value of q^* for the next value of α . The third group are simulations that were designed using extrapolations of q^* from measurements at $\alpha \leq 3.75$. For model S2-64, the first group corresponds to the simulations designed to be commensurate with the RPA prediction of q^* . The second group utilizes SCFT for designing the simulation box. The third group utilizes extrapolated values of q^* from lower χN .

(a) Model S1-64

α	χN	M	NM	$N_{\rm step} \times 10^{-6}$
0	0	3403	217792	66
0.5	8.0	3403	217792	66
1	16.7	3403	217792	66
1.5	25.7	3403	217792	66
1.75	30.3	3403	217792	66
2.0	35.0	3403	217792	66
2.25	39.7	4091	261824	51
2.5	44.5	4624	295936	51
2.75	49.2	4805	307520	51
3	54.0	5086	325504	215
3.25	58.8	5373	343872	220
3.5	63.7	5673	363072	175
3.75	68.5	6037	386368	115
4.0	73.4	6372	407808	95
4.25	78.3	6672	427008	95
4.5	83.2	6966	445824	125
5	93	7529	481856	90

(b) Model S2-64

α	χN	М	NM	$N_{\rm step} \times 10^{-6}$
0	0	6803	435392	30
1.5	8.6	6803	435392	27
3.5	19.5	6803	435392	27
4.5	24.8	6803	435392	27
5.5	29.6	6803	435392	27
6	32.4	6803	435392	57
6.5	34.8	6803	435392	57
7	37.2	10149	649536	87
7.5	39.6	9194	588416	87
8	41.9	9081	581184	87
9	46.5	8879	568256	313
10	50.9	9384	600576	117
11	55.2	10306	659584	120

B. Spontaneous melting and crystallization

For all simulations that were designed to study spontaneous crystallization and melting, the box size was designed to yield a primary Bragg scattering peak commensurate with a value of q^* in the disordered phase at the same value of α . Simulations of both models were carried using values of M that were chosen to accommodate either a $3 \times 3 \times 3$ or a $2 \times 2 \times 2$ array of BCC cubic unit cells. For most such simulations, the estimate of q^* required to compute M was obtained from a previous simulation performed at the same value of α that was used to measure properties of the disordered phase, for which the value of M had been chosen using one of the more approximate strategies described above. The resulting measurement of q^* at each value of α was then used to compute a refined estimate of M for a commensurate system, which was then used to design separate simulations that were used only to study crystallization and melting. The only exception to this are the simulations at $\alpha = 8.5$ for Model S2-64, for which the box size was calculated by interpolating the value of q^* from the value at $\alpha = 8$ and 9. Table S2 lists the parameters used in these studies of crystallization and melting.

TABLE S2: Parameters for simulations used to study spontaneous melting and crystallization, where M is the number of chains of N=64 beads. Subtables show data for models (a) S1-64 and (b) S2-64. Horizontal lines separate $2\times 2\times 2$ and $3\times 3\times 3$ systems. In the last column, $I \xrightarrow{n} F$ indicates a simulation of n million MD steps with initial state I and final state F, with state values to C for crystal and D for disordered.

(a) Model S1-64

α	χN	BCC cells	М	simulation
2.75	49.2	$2 \times 2 \times 2$	1434	$C \xrightarrow{80} D, D \xrightarrow{80} D$
3	54	$2 \times 2 \times 2$	1521	$C \xrightarrow{120} D, D \xrightarrow{120} D$
3.25	58.8	$2 \times 2 \times 2$	1624	$C \xrightarrow{120} C, D \xrightarrow{120} C$
3.25	58.8	$3 \times 3 \times 3$	5373	$C \xrightarrow{60} D$
3.5	63.7	$3 \times 3 \times 3$	5542	$C \xrightarrow{55} D$
3.75	68.5	$3 \times 3 \times 3$	6025	$C \xrightarrow{90} C, D \xrightarrow{110} D$
4	73.4	$3 \times 3 \times 3$	6372	$C \xrightarrow{90} C$

(b) Model S2-64

α	χN	BCC cells	M	simulation
7.5	39.6	$2 \times 2 \times 2$	2513	$C \xrightarrow{100} D, D \xrightarrow{100} D$
8	41.9	$2 \times 2 \times 2$	2553	$C \xrightarrow{100} D, D \xrightarrow{100} D$
8.5	44.2	$2 \times 2 \times 2$	2609	$C \xrightarrow{200} C, D \xrightarrow{100} C$
9	46.5	$2 \times 2 \times 2$	2665	$C \xrightarrow{100} C, D \xrightarrow{350} C$
10	50.9	$2 \times 2 \times 2$	2781	$C \xrightarrow{100} C, D \xrightarrow{100} C$
7.5	39.6	$3 \times 3 \times 3$	8481	$C \xrightarrow{40} D, D \xrightarrow{40} D$
8	41.9	$3 \times 3 \times 3$	8615	$C \xrightarrow{40} D, D \xrightarrow{80} D$
8.5	44.2	$3 \times 3 \times 3$	8805	$C \xrightarrow{80} D, D \xrightarrow{80} D$
9	46.5	$3 \times 3 \times 3$	8995	$C \xrightarrow{80} C, D \xrightarrow{80} D$
10	50.9	$3 \times 3 \times 3$	9384	$C \xrightarrow{120} C$
11	55.2	$3 \times 3 \times 3$	10306	$C \xrightarrow{120} C$

III. STRUCTURE FACTOR

The structure factor $S(\mathbf{q})$ evaluated at a wavevector \mathbf{q} is defined as

$$S(q) = \left\langle \frac{1}{V} |\tilde{\psi}(\mathbf{q})|^2 \right\rangle \quad , \tag{S1}$$

in our simulation, where V is total system volume, $\tilde{\psi}(\mathbf{q}) = \int d\mathbf{r} \ \psi(\mathbf{r}) e^{i\mathbf{q}\cdot\mathbf{r}}$ is a Fourier amplitude of a composition field $\psi(\mathbf{r}) = [c_A(\mathbf{r}) - c_B(\mathbf{r})]/2$, and $c_i(\mathbf{r})$ is the concentration of i monomers. The Fourier amplitude $\tilde{\psi}$ may also be written more concretely in terms of bead positions as a sum

$$\tilde{\psi}(\mathbf{q}) = \frac{1}{2} \sum_{j} \epsilon_{j} e^{i\mathbf{q} \cdot \mathbf{R}_{j}}$$
 (S2)

where j is a bead index, \mathbf{R}_j is the position of bead j, the sum is taken over all beads of all chains in the system, and ϵ_j is a coefficient that is equal to +1 for beads of type A and equal to -1 for beads of type B. The values of S(q) shown in the main text are averages over time and over all members of a family of wavevectors of equal magnitude $q = |\mathbf{q}|$ that are related by cubic symmetries.

A hierarchial block averaging analysis [9] is used to find the average S(q) for different values of q. An instantenous S(q) averaged over the wavevectors within the same family (wavevectors related by cubic symmetry) is first calculated every 1000 timesteps. The whole sequence is then divided into blocks consisting of 2^n contiguous measurements for blocking level n, for $n = 0, 1, 2, \ldots$ A block average value of S(q) is then calculated for each block. Using these block average values, a standard error is calculated by treating the block averages as if they were statistically uncorrelated. For small n, neighboring values within the sequence of block averages may be strongly correlated. However, given a long enough sequence, consistent error estimates will be obtained for sufficiently large n as block averages for larger blocks become uncorrelated. The existence of a "plateau" in error estimates obtained from different block lengths, in which different values of n yield consistent values, indicates that the sequence is long enough to yield ergodic sampling, and yields an estimated statistical error on S(q) that is given by the plateau value.

Simulations lengths used here were chosen so as to obtain ergodic sampling of the primary peak since the Fourier amplitude associated with this peak has been found to relax most slowly. Lack of ergodic sampling can also be diagnosed by the existence of time averages of $S(\mathbf{q})$ for different wavevectors within the family of symmetry-related wavevectors that correspond to the peak in S(q) that differ by more than apparent statistical errors.

Estimated values of the peak intensity $S(q^*)$ and peak wavenumber q^* have been extracted from a fit of an RPA function form to the peak in the averaged S(q), as described in the main text. Table S3 shows the resulting values $S(q^*)$ and q^* obtained at different χN for simulations using model S1-64. The corresponding table for model S2-64 can be found in the supplementary material of Ref. [10]. An estimate of the error on $S(q^*)$ is calculated using the root mean squared deviation of S(q) from the fit for values of q within 10% of q^* .

α	χN	$S(q^*)/cN$	q^*R_{g0}
0	0	0.010 ± 0.000005	2.355
0.5	8.0	0.013 ± 0.00001	2.329
1	16.7	0.016 ± 0.00002	2.293
1.5	25.7	0.023 ± 0.000001	2.257
1.75	30.3	0.029 ± 0.00003	2.226
2	35.0	0.040 ± 0.00007	2.196
2.25	39.7	0.065 ± 0.0003	2.128
2.5	44.4	0.125 ± 0.001	2.075
2.75	49.2	0.255 ± 0.0003	2.019
3	54.0	0.460 ± 0.0002	1.980
3.25	58.8	0.733 ± 0.007	1.937
3.5	63.7	1.071 ± 0.008	1.930
3.75	68.5	1.349 ± 0.042	1.877

TABLE S3: Nondimensionalized peak intensity $S(q^*)/cN$ and peak wavenumber qR_{g0} at different values of α or χN for model S1-64 ($\overline{N}=960$).

IV. PHASE TRANSITIONS AND THERMODYNAMICS

A. Order-Disorder Transition Temperature

We have also performed simulations to identify conditions under which an initially disordered melt will spontaneously crystallize or an initially ordered crystal will spontaneously melt in systems that are designed so that the periodic simulation unit cell is, as nearly as possible, commensurate with the preferred crystallographic unit cell. Such simulations were performed for both values of \overline{N} using systems in which the number of molecules was chosen so as to accommodate either 27 cubic BCC unit cells and 54 micelles in a $3 \times 3 \times 3$ arrangement or 8 cubic unit cells and 16 micelles in a $2 \times 2 \times 2$ arrangement.

For each such simulation, the number of molecules was chosen so that a crystal with the desired configuration yields a primary BCC Bragg scattering peak with a wavevnumber equal to the peak wavenumber q^* found in a simulation of the disordered phase at the same value of α . At each selected value of α or χN , we performed either a simulation that was initialized in a disordered phase or a simulation initialized in an ordered BCC lattice, or both. Crystalline initial states were generated by performing short preliminary simulations using a modified potential energy that includes an external field that attracts minority block monomer to regions near the expected positions of the micelle cores [10]. The final state of each such preliminary simulation is then used as the initial state of longer simulation performed without any external field.

We first discuss simulations for $\overline{N}=960$. Simulations of systems designed to accommodate a $2\times2\times2$ array of unit cells exhibited spontaneous melting of an artificially ordered BCC initial state at $\chi N \leq 54.0$ ($\alpha \leq 3.0$) and spontaneous crystallization of a BCC phase from a disordered initial state at $\chi N \geq 58.8$ ($\alpha \geq 3.25$). The equilibrium crystallization temperature for this very small system presumably lies between these bounds. Simulations of initially ordered states with a $3\times3\times3$ arrangement of unit cells exhibited spontaneous melting at $\chi N \leq 63.7$ ($\alpha \leq 3.5$). Simulations of initially disordered $3\times3\times3$ systems did not crystallize at any value of χN studied here. Moreover, we were able to obtain apparently ergodic sampling of the disordered phase of $3\times3\times3$ systems for this model only for $\chi N \leq 68.5$ ($\alpha \leq 3.75$).

Results of simulations of systems with $\overline{N}=3820$ have been reported previously [10] and

are reviewed here. Simulations of $2 \times 2 \times 2$ crystals were found to exhibit spontaneous melting of a crystal initial state for $\chi N \leq 41.9$ ($\alpha \leq 8$) and exhibited spontaneous crystallization of an initially disordered state for $\chi N \geq 44.2$ ($\alpha \geq 8.5$). Simulations of $3 \times 3 \times 3$ systems exhibit spontaneous melting for $\chi N \leq 44.2$ ($\alpha \leq 8.5$) but did not exhibit spontaneous crystallization for any conditions that we studied. Note that we have now run simulations at $\chi N = 44.2$ ($\alpha = 8.5$) that allows us to report better lower bounds on the ODT as reported in our previous work [10]. For this model, we were able to obtain apparently ergodic sampling of the disordered phase only for $\chi N \leq 46.5$ ($\alpha \leq 9$) [10].

Comparison of results for the $2 \times 2 \times 2$ and $3 \times 3 \times 3$ systems for $\overline{N} = 960$ indicates the existence of a substantial effect of finite system size on the location of the equilibrium transition, in which finite size effects appear to favor the formation of an ordered phase. Note that the lower bound of $(\chi N)_{\text{odt}} > 63.7$ found for the $3 \times 3 \times 3$ system is outside the range $54.0 < (\chi N)_{\text{odt}} < 58.8$ obtained from simulations of $2 \times 2 \times 2$ systems. This suggests that $2 \times 2 \times 2$ systems are simply too small to be used for quantitative studies of crystallization. We assume (but cannot prove) that the importance of finite size effects decreases rapidly with further increases in system size, and the value of χN at the equilibrium transition for a $3 \times 3 \times 3$ system lies much closer to that of an infinite system.

In light of the fact that we observe spontaneous melting but not spontaneous crystallization in $3 \times 3 \times 3$ systems for both models, we believe that the lower bound provided by spontaneous melting of initially ordered $3 \times 3 \times 3$ systems provides the best estimate of the equilibrium value of $(\chi N)_{\text{odt}}$ available from these simulations. This estimate yields $(\chi N)_{\text{odt}} \simeq 63.7$ for $\overline{N} = 960$ and $(\chi N)_{\text{odt}} \simeq 44.2$ for $\overline{N} = 3820$, which may be compared to the SCFT prediction $(\chi N)_{\text{odt}}^{\text{scf}} = 36.6$. If we assume that the CMT lies proximate to the $(\chi N)_{\text{odt}}^{\text{scf}}$ [10, 11], then these results clearly demonstrate the existence of a disordered micellar state over a wide range of values of χN for the lower value of $\overline{N} = 960$, and suggest that $(\chi N)_{\text{odt}}$ increases rather rapidly with decreasing \overline{N} for sphere-forming systems.

B. Free Energy

Earlier simulation studies [1, 2, 4] of more symmetric diblock copolymers have characterized thermodynamics by considering the dimensionless free energy per chain $g = G/(Mk_BT)$ and its derivative $g' \equiv \partial g/\partial(\chi N)$, in which G is total Gibbs free energy of a system of M

polymers. Both g' and g can be computed from simulation data using a theorem that relates the derivative $\partial g/\partial \alpha$ to the A-B pair energy in an NPT simulation [1, 2]. The derivative g'is a universal function of χN and \overline{N} that is also proportional to the AB pair energy, and thus provides a dimensionless measure of the amount of contact between A and B monomers. For reference, SCFT predicts that g' = f(1 - f) in a disordered phase of a diblock copolymer with minority block fraction f.

Figure S1 shows the variation in g' with χN as well as SCFT predictions of g' both for the FCC phase and BCC phases for $\chi N > (\chi N)_{\rm odt}^{\rm scf}$. A striking feature in this plot is the close agreement between (i) measured values of g' in both the disordered phase near the ODT and the ordered phase and (ii) SCFT predictions for the ordered phase at the same value of χN . These observations are consistent with conclusions of previous simulation studies [1, 2, 4] of symmetric and more modestly asymmetric diblock copolymers, which have generally shown that predictions of SCFT for an ordered phase at $\chi N > (\chi N)_{\rm odt}^{\rm scf}$ provides reasonable predictions for thermodynamic properties of both ordered phases and disordered but strongly-segregated phases.

C. Latent Heat

The difference between the values of g' in coexisting disordered and ordered phases can be related to the heat of transition. Let $\Delta h = \Delta H/(MkT)$ denote the non-dimensional heat of transition per molecule, where ΔH is the difference between the enthalpies of the disordered and ordered phases of a system of M molecules. Let $\Delta g'$ denote the corresponding difference between values of g' in the ordered and disordered phases. It has been shown [12] that these quantities are related by a simple proportionality

$$\Delta h = A \Delta g' \quad , \tag{S3}$$

in which $A = \partial \chi / \partial (1/T)$.

One useful way to characterize latent heat is to report either Δh or $\Delta g'$ as a percentage of the value of h or g' in the disordered phase at a transition. Prior work [1, 2] on simulations of the lamellar-disorder transition of symmetric diblock copolymers, for which $(\chi N)_{\text{odt}}$ was determined very accurately, showed that these systems exhibit a 6-7 % change in h or g' at the transition, over a relatively wide range of values of \overline{N} . For sphere-forming systems of

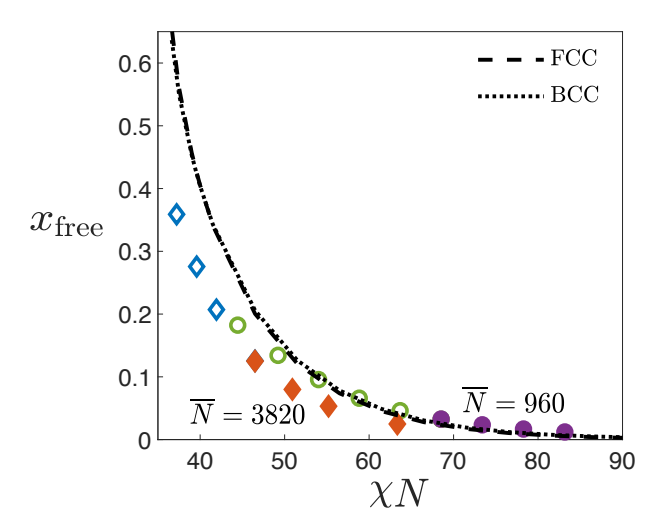


FIG. S1: Free energy derivative $g' = \partial g/\partial(\chi N)$ vs χN . Open symbols show results obtained in the disordered phase and closed symbols are results obtained in an ordered phase that remains stable (i.e., does not spontaneously melt). The horizontal solid line plotted for $\chi < (\chi N)_{\rm odt}^{\rm scf}$ gives the SCFT prediction of g' = f(1-f) = 7/64 for the randomly mixed disordered phase. The dashed line and the dotted lines are SCFT predictions of the FCC and the BCC phase respectively. The difference between the latter two curves is so small that the curves are essentially indistinguishable. On increasing χN from the disordered phase, g' jumps from 7/64 to the SCFT prediction of the crystal phase at the $(\chi N)_{\rm odt}^{\rm scf}$.

interest here, we do not know the exact value of $(\chi N)_{\rm odt}$. We can, however, compute the difference between value of g' in the ordered and disordered phases at a value of χN at or near the lowest value for which the BCC ordered remained stable in simulations designed to study spontaneous melting. For $\overline{N}=960$ we find a fractional difference of 1.14% at $\chi N=68.5$ and a difference of 0.58% at $\chi N=73.4$. For $\overline{N}=3820$ we obtain a fractional difference of 0.93% at $\chi N=46.5$ and 0.91% at $\chi N=50.9$.

There are significant uncertainties in our estimates of Δh in sphere-forming systems, both because of the sensitivity of the results to small changes in the unit cell parameters (which may not be exactly optimal in our simulations) and because of uncertainty in the value of $(\chi N)_{\rm odt}$ for these systems. The available results suggest, however, that the order-disorder transition of sphere-forming diblock copolymers is associated with a much smaller fractional change in enthalpy than that found for symmetric diblock copolymers. This qualitative

observation is consistent with experimental observations of much smaller latent heats for sphere-forming diblock copolymers than for nearly symmetric copolymers [13]. The change in enthalpy upon crystallization of a system of spherical micelles is very closely related to a corresponding change in the area of contact A and B monomers along interfaces surrounding the micelle cores. The observation of a small latent heat is consistent with a picture of the order-disorder transition as a crystallization transition that is accompanied by very little change in the distribution of sphere aggregation numbers, and thus very little change in the amount of AB contact area per unit volume.

V. DYNAMICS OF INTER-MICELLE BRIDGES

This section discusses the analysis of the dynamics of the creation and destruction of transient bridges that form between nearest neighbor micelles within the ordered phase. The first subsection discusses a mathematical model that relates rate constants for bridge creation and destruction to the autocorrelation function for the number of bridges between nearest-neighbor micelles in a simulation of a micelle crystal. The second subsection presents results in which this model has been used to analyze our data.

A. Mathematical model

Consider a BCC crystal consisting of N_m micelles and N_b possible bridges forming between nearest neighbors. Because each micelle in a BCC crystal has 8 nearest neighbors, and each nearest neighbor bond is shared by two micelles, $N_b = 4N_m$, where $N_m = 54$ for a simulation cell holding $3 \times 3 \times 3$ BCC cubic unit cells.

Suppose that we label each of the N_b nearest neighbor bonds in the system by a unique integer index index $i = 1, ..., N_b$. We also assign each such bond a stochastic Boolean variable $m_i(t)$ such that $m_i(t) = 1$ if a bridge exists along bond i at time t and $m_i(t) = 0$ if no such bridge exists. Let M(t) denote the total number of active bridges at time t, which is given by a sum

$$M(t) = \sum_{i=1}^{N_b} m_i(t) \quad . \tag{S4}$$

We assume in what follows that values of $m_i(t)$ for different bonds are statistically independent, and therefore

$$\langle \delta M(t)\delta M(0)\rangle = N_b \langle \delta m(t)\delta m(0)\rangle$$
 , (S5)

where $\delta M(t) \equiv M(t) - \langle M \rangle$, $\delta m(t) = m(t) - \langle m \rangle$, and $\langle \delta m(t) \delta m(0) \rangle$ is an autocorrelation function for the Boolean variable associated with any one of the N_b identical bonds. Our goal is to relate the behavior of $\langle M(t)M(0) \rangle$ to the characteristic rates for creation and destruction of bridges.

The quantity m(t)m(0) is 1 for systems in which m(0) = m(t) = 1 and zero otherwise. The average of this quantity may thus be expressed as a product

$$\langle m(t)m(0)\rangle = G_1(t)\langle m\rangle$$
 (S6)

in which $\langle m \rangle$ is the equilibrium probability of finding m=1 at time t=0, which is also equal to the fraction of active bridges, and $G_1(t)$ is the conditional probability that a bridge for which m=1 at t=0 also has m=1 at a later time t. The corresponding value of

$$\langle \delta m(t)\delta m(0)\rangle = \langle m(t)m(0)\rangle - \langle m\rangle^2$$
 (S7)

is thus

$$\langle \delta m(t) \delta m(0) \rangle = \langle m \rangle [G_1(t) - \langle m \rangle] \quad . \tag{S8}$$

Note that we expect $G_1(t) \to \langle m \rangle$ as $t \to \infty$, giving $\langle \delta m(t) \delta m(0) \rangle \to 0$ in this limit.

Consider an ensemble of bridges in which the probability of a randomly chosen bridge being in state n at time t is given by $P_n(t)$, for n = 0 and n = 1. These probabilities obey the system of differential equations

$$\frac{dP_0(t)}{dt} = -cP_0 + dP_1$$

$$\frac{dP_1(t)}{dt} = +cP_0 - dP_1 \quad ,$$

in which c and d are rate constants for bridge creation and destruction, respectively. Let values $P_n^{(eq)}$ with n=0 and n=1 denote corresponding equilibrium probabilities, toward which the above time dependent probabilities evolve as $t \to \infty$. Combining the detailed balance condition $cP_0^{(eq)} = dP_1^{(eq)}$ with the normalization condition $P_0^{(eq)} + P_1^{(eq)} = 1$ yields an equilibrium bridge probability

$$\langle m \rangle = P_1^{(eq)} = \frac{c}{d+c} \quad . \tag{S9}$$

and $P_0^{(eq)} = 1 - P_1^{(eq)} = d/(d+c)$.

The above system of ODEs for $P_n(t)$ can be formulated as a matrix problem

$$\mathbf{P}(t) = \mathbf{RP}(t) \tag{S10}$$

in which $\mathbf{P}(t)$ is a column vector $\mathbf{P}(t) = [P_0(t) \quad P_1(t)]^T$ and where \mathbf{R} is a matrix

$$\mathbf{R} = \begin{bmatrix} -c & d \\ c & -d \end{bmatrix} \quad . \tag{S11}$$

The eigenvalues of \mathbf{R} are $\lambda = 0, -c - d$ and the general solution to the system of ODE's with a normalized initial condition is

$$\begin{bmatrix} P_0(t) \\ P_1(t) \end{bmatrix} = \frac{1}{c+d} \begin{bmatrix} d \\ c \end{bmatrix} + \frac{B}{c+d} \begin{bmatrix} 1 \\ -1 \end{bmatrix} e^{-(c+d)t} , \qquad (S12)$$

where the two column vectors on the right-hand side are eigenvectors of \mathbf{R} , and where B is an arbitrary parameter that must be chosen to satisfy initial conditions.

Let $G_n(t)$ denote the conditional probabilities of finding a bond that was in a known state m = 1 at t = 0 having a value m(t) = n at time t, for n = 0 and n = 1. This conditional probability is the solution to the above system of ODEs with initial conditions $G_0 = 0$ and $G_1(0) = 1$ This initial condition is satisfied by setting B = -d, giving

$$G_1(t) = \frac{1}{c+d} \left[c + de^{-(c+d)t} \right]$$
 (S13)

Note that $G_1 = 1$ at t = 0 as required by the initial condition, and $G_1 \to c/(c+d) = \langle m \rangle$ as $t \to \infty$.

Combining results for $G_1(t)$ and $\langle m \rangle$ then gives

$$\langle \delta m(t)\delta m(0)\rangle = \frac{cd}{(c+d)^2}e^{-(c+d)t}$$
 (S14)

or, equivalently,

$$\langle M(t)M(0)\rangle = N_b \frac{cd}{(c+d)^2} e^{-(c+d)t} \quad . \tag{S15}$$

Let F(t) denote a reduced autocorrelation function

$$F(t) \equiv \frac{\langle \delta M(t) \delta M(0) \rangle}{\langle \delta M(0) \delta M(0) \rangle} \quad . \tag{S16}$$

This model predicts

$$F(t) = e^{-(c+d)t} = e^{-t/\tau}$$
 , (S17)

where $\tau = 1/(c+d)$ is the bridge lifetime.

The autocorrelation function $\delta M(t)\delta M(0)\rangle$ can be computed by first finding the number of bridges at time t by identifying the cluster multiplets using the 2D histogram analysis. In the total number of bridges forming in the simulation, every micelle dimer contributes 1 bridge and a trimer contributes 2 bridges. Similarly, we can find the contribution of higher order cluster multiplets. Using the resulting values of M(t) at different t, we can compute $\langle M(t)M(0)\rangle$ and F(t). The above model predicts that F(t) should decay exponentially with a decay time equal to the bridge lifetime τ .

B. Results

The first step in our analysis of bridge lifetime is to compute the number M(t) of bridges at the system for a sequence of trajectory snapshots that are evenly spaced in time. We

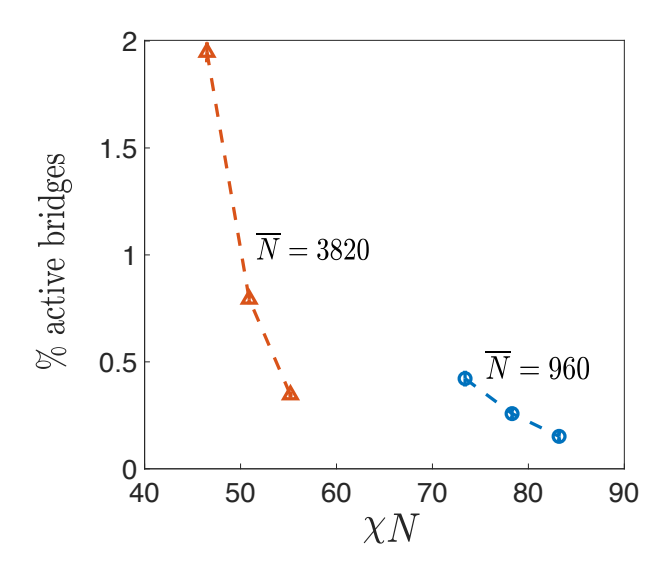


FIG. S2: Percentage of active bridges (i.e., percent of nearest-neighbor bonds along which there exists a bridge) vs. χN for crystal phases of both models.

sample the trajectory every 1000 steps, apply a cluster analysis to each such snapshot to identify the number of micelle, unimers, dimers, trimers, etc. To compute M(t), we assume that the number of bridges in each multimer is one less than the number of micelles, giving one bridge per dimer, two per trimer, etc. Because we assume that bridges can only be formed between the nearest neighbors, and we know the number of nearest neighbor bonds, we can compute the percentage of nearest-neighbor bonds along which bridges exist. This fraction is shown in Figure S2 for crystalline states of models with $\overline{N} = 960$ and 3820.

Given a sequence of values of M sampled at regular intervals, it is straightforward to compute values of F(t) at values of t corresponding to integer multiples of the sampling interval. Figures S3 and S4 show the behavior of F(t) on time t for $\overline{N} = 960$ and 3820 at several values of χN . Figure S3 shows the behavior of F(t) at early times that differ by our sampling interval of 1000 time steps. Note that the value F(t) at the first nonzero sampled time, corresponding to 1000 time steps, is substantially less than 1. This implies that a substantial fraction of the bridges that are present in a given snapshot have been destroyed before the next sampled snapshot. The fraction of very short-lived bridges that survive less than 1000 time steps is significantly greater for $\overline{N} = 3280$ than for $\overline{N} = 960$. Figure S4 shows the behavior F(t) for both models for much longer times. Results for F(t) at t > 0, excluding the initial value F(0) = 1, have been fit to a double exponential function

$$F(t) = K_1 e^{-t/\tau_1} + K_2 e^{-t/\tau_2} \quad , \tag{S18}$$

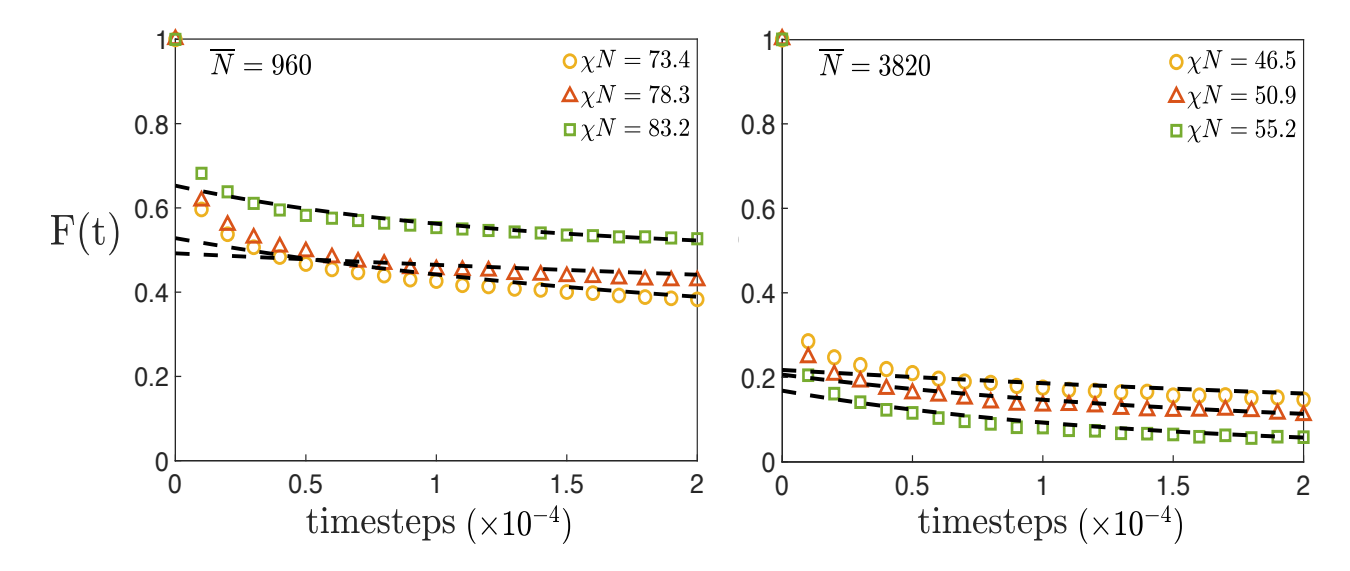


FIG. S3: Time dependence of F(t) at early times in micelle crystals at several values of χN . Values of F(t) are shown at integer multiples of the sampling interval of 1,000 time steps. Dashed lines show fits of data for t > 0 to Eq. (S18).

where K_1 and K_2 are dimensionless coefficients and τ_1 and τ_2 are decay times, with $\tau_1 < \tau_2$. Results of this fit are shown as dashed lines in Figure S4. The shorter decay time τ_1 in these fits is of order 10^4 time steps while the longer time τ_2 is several times 10^5 time steps. Thus, while many bridges are very short-lived, it appears that there exists a subset of bridges with much longer lifetimes.

To construct Fig. 18 of the main manuscript, we have arbitrarily classified each micelle dimer as "long-lived" if it is found to exist along a given bond for two or more consecutive samples, which are separated by a sampling interval of 1000 time steps, and as "short-lived" if a dimer was found along a specific bond only in one sample, and not in preceding or subsequent samples. Figure 18 shows effective cross-sectional radii as functions of distance z along the long axis for the resulting sets of short-lived and long-lived dimers.

J. Glaser, P. Medapuram, T. M. Beardsley, M. W. Matsen, and D. C. Morse, Universality of block copolymer melts, Phys. Rev. Lett. 113, 068302 (2014).

^[2] P. Medapuram, J. Glaser, and D. C. Morse, Universal phenomenology of symmetric diblock copolymers near the order-disorder transition, Macromolecules 48, 819 (2015).

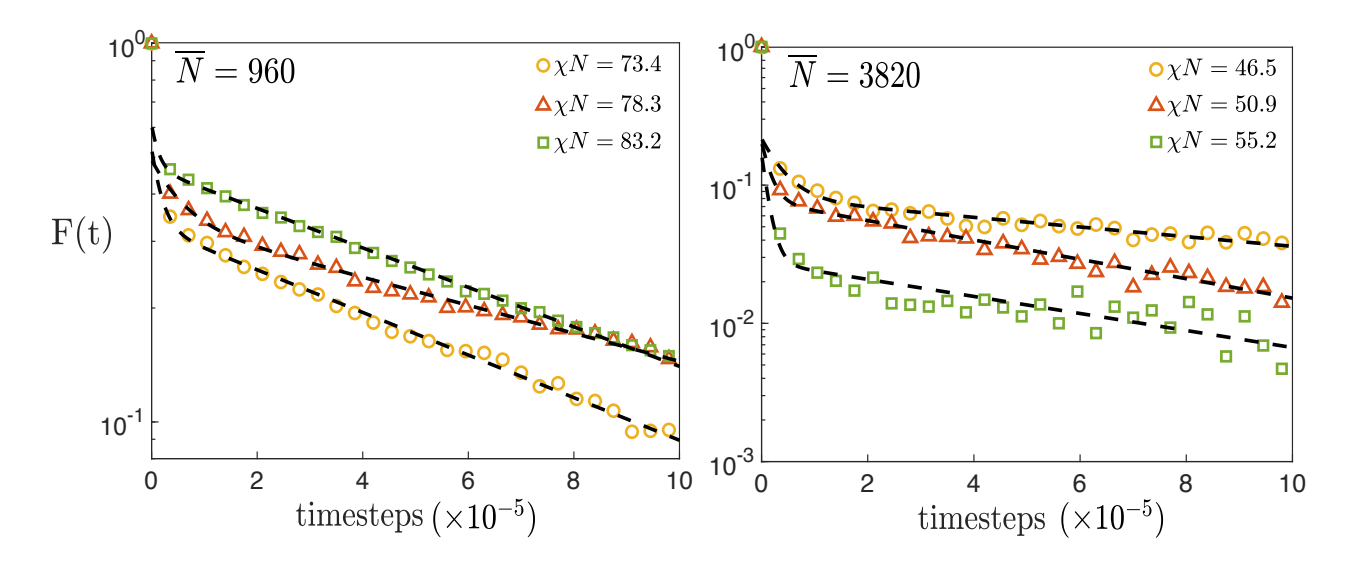


FIG. S4: Semi-logarithmic plot of the time dependence of F(t) at late times in micelle crystals at several values of χN . Dashed lines show the fits to equation (S18). Values of F(t) are shown at intervals separated by 32,000 time steps.

- [3] T. Ghasimakbari and D. C. Morse, Correlations in disordered melts of asymmetric diblock copolymers, Macromolecules **51**, 2335 (2018).
- [4] T. Ghasimakbari and D. C. Morse, Order-disorder transitions and free energies in asymmetric diblock copolymers, Macromolecules **53**, 7399 (2020).
- [5] J. A. Anderson, C. D. Lorenz, and A. Travesset, General purpose molecular dynamics simulations fully implemented on graphics processing units, J. Comput. Phys. **227**, 5342 (2008).
- [6] J. Glaser, T. D. Nguyen, J. A. Anderson, P. Lui, F. Spiga, J. A. Millan, D. C. Morse, and S. C. Glotzer, Strong scaling of general-purpose molecular dynamics simulations on gpus, Comput. Phys. Commun. 192, 97 (2015).
- [7] G. J. Martyna, D. J. Tobias, and M. L. Klein, Constant pressure molecular dynamics algorithms, J. Chem. Phys. **101**, 4177 (1994).
- [8] G. J. Martyna, M. E. Tuckerman, D. J. Tobias, and M. L. Klein, Explicit reversible integrators for extended systems dynamics, Molecular Physics 87, 1117 (1996).
- [9] H. Flyvbjerg and H. Petersen, Error estimates on averages of correlated data, J. Chem. Phys. 91, 461 (1989).
- [10] A. Chawla, F. S. Bates, K. D. Dorfman, and D. C. Morse, Identifying a critical micelle temperature in simulations of disordered asymmetric diblock copolymers, Phys. Rev. Mater. 5,

- L092601 (2021).
- [11] J. Wang, Z.-G. Wang, and Y. Yang, Nature of disordered micelles in sphere-forming block copolymer melts, Macromolecules 38, 1979 (2005).
- [12] T. M. Gillard, P. Medapuram, D. C. Morse, and F. S. Bates, Fluctuations, phase transitions, and latent heat in short diblock copolymers: Comparison of experiment, simulation, and theory, Macromolecules 48, 2801 (2015).
- [13] S. Lee, T. M. Gillard, and F. S. Bates, Fluctuations, order, and disorder in short diblock copolymers, AIChE Journal **59**, 3502 (2013).